

# Learning the Factors Controlling Mineralization for Geologic Carbon Sequestration

Aleksandra Pachalieva<sup>a,b,\*</sup>, Jeffrey D. Hyman<sup>b</sup>, Daniel O'Malley<sup>b</sup>, Hari Viswanathan<sup>b</sup> and Gowri Srinivasan<sup>c</sup>

<sup>a</sup>Center for Nonlinear Studies (CNLS), Theoretical Division, Los Alamos National Laboratory, Los Alamos, 87544, NM, USA

<sup>b</sup>Energy & Natural Resources Security Group (EES-16), Earth and Environmental Sciences Division, Los Alamos National Laboratory, Los Alamos, 87544, NM, USA

<sup>c</sup>X Computational Physics Division, Los Alamos National Laboratory, Los Alamos, 87544, NM, USA

## ARTICLE INFO

### Keywords:

discrete fracture network  
reactive transport  
dissolution  
regression model

## ABSTRACT

We perform a set of flow and reactive transport simulations within three-dimensional fracture networks to learn the factors controlling mineral reactions. CO<sub>2</sub> mineralization requires CO<sub>2</sub>-laden water, dissolution of a mineral that then leads to precipitation of a CO<sub>2</sub>-bearing mineral. Our discrete fracture networks (DFN) are partially filled with quartz that gradually dissolves until it reaches a quasi-steady state. At the end of the simulation, we measure the quartz remaining in each fracture within the domain. We observe that a small backbone of fracture exists, where the quartz is fully dissolved which leads to increased flow and transport. However, depending on the DFN topology and the rate of dissolution, we observe a large variability of these changes, which indicates an interplay between the fracture network structure and the impact of geochemical dissolution. In this work, we developed a machine learning framework to extract the important features that support mineralization in the form of dissolution. In addition, we use structural and topological features of the fracture network to predict the remaining quartz volume in quasi-steady state conditions. As a first step to characterizing carbon mineralization, we study dissolution with this framework. We studied a variety of reaction and fracture parameters and their impact on the dissolution of quartz in fracture networks. We found that the dissolution reaction rate constant of quartz and the distance to the flowing backbone in the fracture network are the two most important features that control the amount of quartz left in the system. For the first time, we use a combination of a finite-volume reservoir model and graph-based approach to study reactive transport in a complex fracture network to determine the key features that control dissolution.

## 1. Introduction

There is increasingly clear evidence of climate change and a strong desire in the research community to combat the effects through techniques such as reducing emissions, carbon dioxide (CO<sub>2</sub>) sequestration, as well as using renewable energy and conserving resources. One of the promising climate change mitigation strategies is CO<sub>2</sub> sequestration, where CO<sub>2</sub> is captured from the atmosphere, and then injected and stored in deep saline aquifers. Injecting large amounts of CO<sub>2</sub> into geologic formations can cause a range of coupled processes such as thermal, mechanical, hydrodynamic, and chemical White, Strazisar, Granite, Hoffman, and Pennline [2003], Gaus [2010], Shao, Ray, and Jun [2010]. This brings the minerals and the waters in the rock formation out of equilibrium, which may cause the dissolution of rock minerals and/or precipitation of secondary minerals and thus change the properties of the pre-existing rock such as morphology, porosity, and permeability. These processes affect the flow and transport of CO<sub>2</sub> and water within the reservoir and are critical for the integrity of the long-term fate of the geologic carbon sequestration (GCS). Therefore, it is critical to understand the geophysical and chemical interactions between minerals and fluids, in order to ensure the efficiency and sustainability of the GCS.

In fairly homogeneous rock formations, reactive fronts can be adequately modeled using reaction rates constrained by elementary principles Maher, Steefel, White, and Stonestrom [2009], Moore, Lichtner, White, and Brantley [2012], Navarre-Sitchler, Steefel, Sak, and Brantley [2011], White, Schulz, Vivit, Blum, Stonestrom, and Anderson

\*Corresponding author

✉ apachalieva@lanl.gov (A. Pachalieva); jhyman@lanl.gov (J.D. Hyman); omalled@lanl.gov (D. O'Malley); viswana@lanl.gov (H. Viswanathan); gowri@lanl.gov (G. Srinivasan)

ORCID(s):

[2008]. However, within fracture networks the application of these simple models is limited, since there exists a highly heterogeneous fluid flow field due to the spatially variable resistance offered to flow by the geo-structural attributes of the fracture network Hyman and Jiménez-Martínez [2018], Hyman, Dentz, Hagberg, and Kang [2019a], Hyman, Jimenez-Martinez, Gable, Stauffer, and Pawar [2020], Maillot, Davy, Le Goc, Darcel, and De Dreuzay [2016], Kang, Hyman, Han, and Dentz [2020], Painter, Cvetkovic, and Selroos [2002], Neuman [2005], Sherman, Hyman, Bolster, Makedonska, and Srinivasan [2018], Sweeney and Hyman [2020], Sweeney, Hyman, O'Malley, Santos, Carey, Stauffer, and Viswanathan [2023], Yoon, Hyman, Han, and Kang [2023]. As readily accessible reactive minerals are depleted, the apparent, or domain-averaged, mineral dissolution rate decreases to values that can be orders of magnitude lower than the laboratory-measured rate Andrews and Navarre-Sitchler [2021], Atchley, Maxwell, and Navarre-Sitchler [2013], Beisman, Maxwell, Navarre-Sitchler, Steefel, and Molins [2015], Jung and Navarre-Sitchler [2018a]. In turn, reactions in fractured media are often transport-controlled and elementary models cannot properly constrain/predict reaction rates Andrews and Navarre-Sitchler [2021], Andrews, Hyman, Sweeney, Karra, Moulton, and Navarre-Sitchler [2023], Berkowitz and Scher [1997], Becker and Shapiro [2000], Edery, Geiger, and Berkowitz [2016], Geiger, Cortis, and Birkholzer [2010], Haggerty, Fleming, Meigs, and McKenna [2001], Huseby, Thovet, and Adler [2001], Hyman, Rajaram, Srinivasan, Makedonska, Karra, Viswanathan, and Srinivasan [2019b], Jung and Navarre-Sitchler [2018a,b], Pandey and Rajaram [2016], Kang et al. [2020], Meigs and Beauheim [2001], Painter et al. [2002], Wen and Li [2018]. Characterizing the feedback between the network structure on the flow field and associated reactive transport requires a coupled thermo-hydro-chemical simulator capable of dynamically modifying flow resistance (hydraulic aperture/permeability) within a three-dimensional fracture network. To date, most computational studies of geochemical reactions have been carried out in a single fracture, small two-dimensional networks, or in upscaled/equivalent continuum models Andrews and Navarre-Sitchler [2021], Andrews et al. [2023], Deng, Molins, Trebotich, Steefel, and DePaolo [2018], Feng, Zhang, Luo, Li, and Du [2019], Lebedeva and Brantley [2017], Jones and Detwiler [2019], Molins, Trebotich, Arora, Steefel, and Deng [2019], Noiriél, Seigneur, Le Guern, and Lagneau [2021], Pandey and Rajaram [2016], Steefel and Lichtner [1998], Steefel and Lasaga [1994], Steefel and Hu [2022]. These three-dimensional high-fidelity simulations, although heavily sought after, were relatively infeasible due to computational limitations. However, recent developments in high-performance computing now allow for the exploration of flow and reactive transport properties in 3D fractured media Hyman, Navarre-Sitchler, Andrews, Sweeney, Karra, Carey, and Viswanathan [2022a].

Machine learning (ML) techniques have shown tremendous promise in geosciences due to the ability to infer parameters and mechanisms of importance with relatively low computational burden. Previous research has exploited ML algorithms to construct reduced order models (ROM) which once trained, can run in a fraction of the time it takes to solve complex advection-dispersion-reaction (ADR) equations Santiago, Velasco-Hernández, and Romero-Salcedo [2014], Goetz, Brenning, Petschko, and Leopold [2015], Valera, Guo, Kelly, Matz, Cantu, Percus, Hyman, Srinivasan, and Viswanathan [2018a]. However, this is only possible because problems including characterizing CO<sub>2</sub> mineralization lend themselves very easily to being represented on a lower dimensional manifold. Flow and transport through fractured rock often happen in preferential pathways where the majority of the reservoir does not participate in the first-order physics. The backbone of the fracture network where the majority of reactive flow takes place is a small fraction of the entire domain of interest. Inferring the characteristics of the backbone prior to solving the ADR yields significant savings in computational time Srinivasan, Karra, Hyman, Viswanathan, and Srinivasan [2019], Viswanathan, J.D., Karra, O'Malley, Srinivasan, Hagberg, and Srinivasan [2018], Vesselinov, Mudunuru, Karra, O'Malley, and Alexandrov [2019], Ahmmed, Mudunuru, Karra, James, and Vesselinov [2021], Liu, Kwon, and Kang [2022]. Structured systems such as fractured rock formations have also been successfully represented as pipes or graphs in previous research, which allows for solving flow and transport equations on the network rather than relying on expensive meshing constructs.

One other benefit of the surrogate models or ROMs obtained through training ML algorithms is their use in a multi-fidelity uncertainty quantification sense. Several thousands to millions of lower fidelity ML algorithms can be used in conjunction with a handful of high fidelity runs to improve both precision and accuracy of the predictions O'Malley, Karra, Hyman, Viswanathan, and Srinivasan [2018].

It is challenging to determine the interplay between the network geostructure and geochemical reactions in fractured media. Even though our physics-based models can simulate these coupled processes, it is difficult to unravel which are the model parameters that control key quantities of interest (e.g. amount of quartz remaining or CO<sub>2</sub> mineralized in a given fracture). In this work, we perform a large number of flow and reactive transport simulations in three-dimensional discrete fracture networks (DFN) to determine the important features that control geochemical mineralization in

the form of dissolution. We isolate the effects of mineral dissolution, by focusing on the simple reaction of quartz dissolution taking into account that this reaction does not induce significant pH changes and will not be sensitive to pH changes in the fluid as other mineral reactions might be. We construct a set of fracture networks composed of a single families of mono-disperse disc-shaped fractures. Initially, the fractures are partially filled with quartz, which dissolves gradually until a quasi-steady state is reached. Depending on the DFN topology and the rate of dissolution, we observe large discrepancies in the remaining quartz in each fracture at the end of the reactive transport simulation. This indicates an interplay between the fracture network structure and the impact of geochemical dissolution, which we would like to understand better. Determining where dissolution or precipitation occurs in a network is critical since they could be positive or negative feedbacks to the flow. Some fractures may flow better allowing for more access to the formation in the case of dissolution. For precipitation, fractures may clog blocking parts of the reservoir. To achieve this, we combine graph representation of the DFNs and machine learning techniques, that allow us to predict the remaining quartz volume in quasi-steady state conditions using the following three categories of features of the fracture network: topological, geometric, and hydrological. By using a regression model, we are also able to assess the importance of different features that characterize the fracture networks. We observe that the most important features are the topological and geometric features, and they are sufficient to train a regression model that predicts the remaining quartz volume in the system. We chose the remaining quartz volume as quantity of interest in our study, because it tells us where most of the reaction is taking place. The distance to the backbone and the rate constant are the features which significantly affect the amount of quartz remaining in each fracture, which is understandable since they control the flow channelization and the strength of the chemical reaction, respectively. The hydrological quantities are the least important ones with respect to the amount of quartz remaining in the system; however, including them in the training process leads to improved confidence in the regression model.

For future work, we aim to simulate the effects of precipitation and dissolution together to be able to fully characterize carbon mineralization. However, looking at dissolution is the first step in testing out this framework.

In Section 2, we describe the methods used to generate the DFNs and simulate flow and reactive transport, as well as the machine learning methods we use. Additionally, we introduce the important features (geometrical, topological, and hydrological) that we use to characterize the fracture networks. In Section 3, we describe the main results of our work, including the random forest model training and testing results, as well as the results from an extensive grid search. In Section 4, we discuss the implications of our results and provide conclusions.

## 2. Methods: Computational Approach

Our primary goal is understanding the connection between properties of the fracture network (topological, geometric, and hydraulic) and resulting geochemical reactions within the network. Identifying such connections is difficult because of the complexity of both the fracture network structure and its impact on fluid flow properties, which determines transport and subsequent reactions. To do so, we adopt a multi-fidelity computational approach. We consider three-dimensional fracture networks using a discrete fracture network (DFN) method. Discrete fracture network models are distinguished from continuum models in that the fractures are explicitly represented rather than via their upscaled effective properties Davy, Le Goc, and Darcel [2013], Davy, Le Goc, Darcel, Bour, de Dreuz, and Munier [2010], de Dreuz, Darcel, Davy, and Bour [2004], de Dreuz, Méheust, and Pichot [2012], Erhel, de Dreuz, and Poirriez [2009], Hyman, Gable, Painter, and Makedonska [2014], Hyman, Karra, Makedonska, Gable, Painter, and Viswanathan [2015], Flemisch, Fumagalli, and Scotti [2016], Manzo, Edwards, Dogru, and Al-Shaalan [2018], Hyman, Sweeney, Gable, Svyatsky, Lipnikov, and Moulton [2022b]. Due to the disparity between their length and aperture, DFN models represent fractures as co-dimension one objects, e.g., lines in two-dimensional simulations and planes in three-dimensional simulations. Each fracture is assigned a shape, location, orientation, and hydraulic properties based on field site characterization. The individual fractures interconnect to form a network. We characterize these fracture networks in terms of their topological (connectivity), geometrical, and hydrological properties using a graph-based approach Hyman, Hagberg, Osthus, Srinivasan, Viswanathan, and Srinivasan [2018]. Graph-based approaches have been shown to be a critical companion to DFN simulations as they provide a rigorous and interpretable manner in which to link fracture network properties to flow and reactive transport observations Hyman, Hagberg, Srinivasan, Mohd-Yusof, and Viswanathan [2017], Hyman and Jiménez-Martínez [2018], Hyman, Dentz, Hagberg, and Kang [2019c], Hyman [2020], Hyman, Sweeney, Frash, Carey, and Viswanathan [2021], Pachaliev, Sweeney, Viswanathan, Stein, Leone, and Hyman [2023], Srinivasan, Hyman, Osthus, Moore, O'Malley, Karra, Rougier, Hagberg, Hunter, and Viswanathan [2018], Yoon et al. [2023]. Flow and reactive transport within the networks are

simulated using the massively parallel subsurface flow and reactive transport code PFLOTRAN Lichtner, Hammond, Lu, Karra, Bisht, Andre, Mills, and Kumar [2015]. There are a variety of reactive transport simulators available that differ in terms of spatial dimensions, discretization schemes, time integration methods, governing equations, flow simulator capabilities (single-phase Darcy flow, variable saturation Richards flow, multi-phase flow, variable density, non-isothermal, and heterogeneous permeability), transport formulations (advection, mechanical dispersion, molecular diffusion, multi-continuum), and geochemistry options (surface complexation, kinetic mineral precipitation-dissolution, aqueous kinetics, mineral nucleation, mineral solid-solutions). The most common simulators in use today are PHREEQC Parkhurst, Appelo, et al. [2013] (which is the geochemistry engine for HPX Jacques, Simunek, Mallants, and Van Genuchten [2018], PHT3D Prommer, Barry, and Zheng [2003], and OPENGEOSSYS Kolditz, Bauer, Bilke, Böttcher, Delfs, Fischer, Görke, Kalbacher, Kosakowski, McDermott, et al. [2012]), HYTEC van Der Lee, De Windt, Lagneau, and Goblet [2003], ORCHESTRA Meeussen [2003], TOUGHREACT Xu, Spycher, Sonnenthal, Zhang, Zheng, and Pruess [2011], ESTOMP White and Oostrom [2003], HYDROGEOCHEM Yeh and Tripathi [1990], CRUNCHFLOW Steefel [2009], MIN3P Su, Mayer, and MacQuarrie [2021], and PFLOTRAN Lichtner et al. [2015]. A comparison of strengths and weaknesses between the codes is provided in Steefel, Appelo, Arora, Jacques, Kalbacher, Kolditz, Lagneau, Lichtner, Mayer, Meeussen, et al. [2015]. The aforementioned graph-based approaches for network characterization have been combined with machine learning techniques to link geo-structure with flow and transport Valera, Guo, Kelly, Matz, Cantu, Percus, Hyman, Srinivasan, and Viswanathan [2018b], Srinivasan et al. [2019], Srinivasan, Cawi, Hyman, Osthus, Hagberg, Viswanathan, and Srinivasan [2020], but this study marks the first time to do so in the context of reactive transport models.

In the first portion of this section, we describe the geometric simulations for reactive transport modeling in fractured media which are used to generate our data set. Next, we describe our adopted machine learning techniques.

## 2.1. Reactive transport modeling

Our reactive transport modeling through fractured media is broken into two steps. The first step is the generation of an ensemble of generic three-dimensional DFN models. In the DFN methodology, fractures are explicitly represented as planar polygons in space. Each fracture has a stochastically sampled shape, size, and orientation. The fracture interconnects to form a network through which flow occurs. This is in contrast to continuum models, where fractures are represented by their effective properties Sweeney, Gable, Karra, Stauffer, Pawar, and Hyman [2020]. The choice to use a DFN model, rather than a continuum model, is born from the desire to link reactive transport observations directly with fracture attributes. The second step is simulating the flow field and associated reactive transport, which requires a coupled thermo-hydro-chemical simulator capable of dynamically modifying flow resistance (hydraulic aperture/permeability) within a three-dimensional fracture network.

### 2.1.1. Three-Dimensional Discrete Fracture Network Modeling

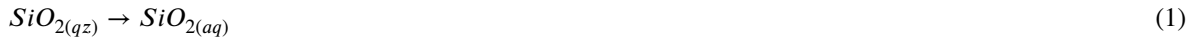
We use DFNWORKS Hyman et al. [2015] software suite to perform our reactive transport simulations in three-dimensional discrete fracture networks (DFN), cf. Viswanathan, Ajo-Franklin, Birkholzer, Carey, Guglielmi, Hyman, Karra, Pyrak-Nolte, Rajaram, Srinivasan, and Tartakovsky [2022] for a comprehensive discussion of DFN modeling approaches. We consider a set of generic networks composed of a single families of mono-disperse (constant sized) disc-shaped fractures in a cubic domain with sides of length 10 meters. Each fracture has a radius of 1.5 meters and their centers are uniformly distributed throughout the domain. Fractures are placed into the domain until a fracture intensity, total surface area over total volume, of  $P_{32} = 3.25$  is obtained. During generation, the domain is increased by 0.5 meters in all directions to mitigate boundary density effects. The orientation of the fracture family is randomly distributed across the unit sphere to mimic a disordered media Hyman and Jiménez-Martínez [2018]. The generic nature of these parameters is designed to isolate the effects of reactive transport and network connectivity from other structural attributes of fracture networks. After generation is complete, we remove isolated fractures, because they do not participate in flow. Once the final network is produced, the feature generation for meshing (FRAM) described in Hyman et al. [2014], which combines network generation with mesh generation to remove features that degrade mesh quality, and the near-Maximal Algorithm for Poisson Sampling (nMAPS) presented in Krotz, Sweeney, Gable, Hyman, and Restrepo [2022], are implemented using the LaGrIT meshing toolbox LaGrIT [2013] to generate a conforming Delaunay triangulation, i.e., the computational mesh. The mesh is composed of uniform triangular elements with edge lengths of 0.05 m. Initially, all fractures are assigned a uniform hydraulic aperture of  $b = 1 \cdot 10^{-5}$  m, which is a reasonable value in crystalline rocks such as granite for fractures of this size Svensk Kärnbränslehantering AB [2010]. The cubic law is used to define the initial permeability of each control volume within the fractures,  $k = 8.3 \cdot 10^{-12}$  m<sup>2</sup>.

Even though the apertures are initially uniform, they can vary spatially. Additional information about the inclusion of in-fracture aperture variability into DFN meshes using DFNWORKS can be found in Karra, Makedonska, Viswanathan, Painter, and Hyman [2015], Frampton, Hyman, and Zou [2019], Makedonska, Hyman, Karra, Painter, Gable, and Viswanathan [2016], Hyman et al. [2021].

### 2.1.2. Flow and reactive transport

Flow and reactive transport within the networks are simulated using the massively parallel subsurface flow and reactive transport code PFLTRAN Lichtner et al. [2015]. Flow in the fracture network is modeled using the Richards equation with a spatially variable permeability field. We use PFLTRAN Lichtner et al. [2015] to numerically integrate the governing equations for pressure and volumetric flow rates. We use a direct method to obtain the solution to the linear system for improved accuracy and performance Greer, Hyman, and O'Malley [2022].

The DFNs are initialized with an 80% volume fraction of quartz ( $\text{SiO}_2$ ) e.g., a uniform fracture porosity of 0.2. Primarily quartz-filled fractures are plausible in crystalline rocks Fisher and Brantley [1992], Navarre-Sitchler, Brantley, and Rother [2015]. A volumetric flow rate boundary condition is applied to the inflow and outflow boundaries of the domain. The flow rate is equal to the initial volume of the particular fracture network per year. Even though the volume of the network increases due to dissolution, this flow rate is held constant. As fresh water is introduced into the domain, the quartz dissolves to produce aqueous silica ( $\text{SiO}_{2(aq)}$ )



The quartz specific surface area ( $A$ ) was defined as  $0.0225 \text{ m}^2 \text{ g}^{-1}$  Wollast and Chou [1988] to calculate the initial total quartz surface area ( $A_o$ ) in each cell. Initial fluid composition in the fractures was in equilibrium with quartz and contained  $1 \cdot 10^{-20} \text{ M}$  non-reactive tracer while the input fluid composition flowing into the domain consisted of  $1 \cdot 10^{-3} \text{ M}$  non-reactive tracer and  $1 \cdot 10^{-20} \text{ M}$   $\text{SiO}_{2(aq)}$ . The non-reactive tracer is used to initialize the transport equations and is not analyzed or considered in this study. We consider four rate constants ( $k$ ) of  $1 \cdot 10^{-9}$ ,  $1 \cdot 10^{-10}$ ,  $1 \cdot 10^{-11}$ ,  $1 \cdot 10^{-12} \text{ mol m}^{-2} \text{ s}^{-1}$ .

The local dissolution rate of quartz ( $R$ ,  $\text{mol m}^{-3} \text{ s}^{-1}$ ) at each time step was calculated according to linear transition state theory (TST),

$$R = kA \left( 1 - \frac{\text{SiO}_{2(aq)}}{K_{eq}} \right), \quad (2)$$

where  $K_{eq} = 10^{-3.9993}$  at  $25^\circ\text{C}$ , as defined in the hanford.dat database distributed with PFLTRAN. As quartz dissolves throughout the simulation, the volume of quartz in each cell is updated and the bulk quartz surface area in each cell is recalculated where  $A$  at time  $t$  is scaled by the ratio of quartz volume ( $V$ ) at time  $t$  and initial quartz volume ( $V_o$ )

$$A_t = \left( \frac{V_t}{V_o} \right)^{2/3} A_o. \quad (3)$$

The permeability, porosity, and mineral surface area of every cell in the mesh are also updated at every time step. Permeability and mineral surface area are updated due to mineral dissolution reactions through the change in porosity

$$\varphi = 1 - \sum_m \varphi_m. \quad (4)$$

Change in permeability involves a phenomenological relation with porosity

$$k = k_0 f(\varphi, \varphi_0, \varphi_c, a), \quad (5)$$

where  $k_0$  is the initial permeability and

$$f = \begin{cases} \left( \frac{\varphi - \varphi_c}{\varphi_0 - \varphi_c} \right)^a & \varphi > \varphi_c, \\ f_{\min} & \varphi \leq \varphi_c \end{cases} \quad (6)$$



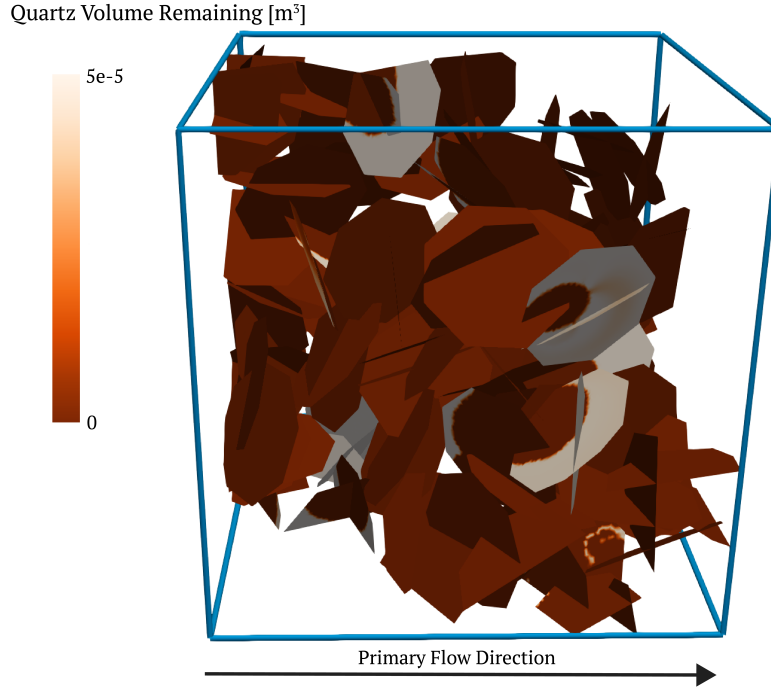


**Figure 1:** DFN containing 59 fractures. Fractures are colored by the remaining total quartz volume in the network at the end of the simulation.

The mineral surface area evolves according to

$$A_m = A_m^0 \left( \frac{\varphi_m}{\varphi_m^0} \right)^n \left( \frac{1 - \varphi}{1 - \varphi_0} \right)^{n'}, \quad (7)$$

where the super/subscript 0 denotes initial values, with a typical value for  $n$  of  $2/3$  reflecting the surface to volume ratio. Note that this relation only applies to primary minerals ( $\varphi_m > 0$ ). The quantity  $\varphi_c$  refers to a critical porosity below which the permeability is assumed to be constant with scale factor  $f_{\min}$ . Note that because hydraulic aperture is integrated into the cell volume which does not change, it is not directly updated at every step. However, these changes in porosity and permeability would correspond to an implicit change in hydraulic aperture with constant porosity under the assumption of a dependency of permeability on the hydraulic aperture. Flow simulations are run for 10 million years, whence all simulations have reached a quasi-steady state in terms of the outflowing  $SiO_{2(aq)}$  values.

At the end of the simulation, we measure the quartz remaining in each fracture within the domain. We consider both the total quartz volume [ $m^3$ ] and the quartz volume fraction, which is the total quartz volume divided by the fracture volume. Figure 1 shows one DFN from our ensemble. Fractures are colored by the total quartz volume remaining at the end of the simulation.

## 2.2. Machine Learning Methods

In this study, our data set is built of the fractures from 800 networks, each executed using one of the four rate constants as defined in Section 2.1.2. The data set is divided into a training set and a test set. We are using a random forest regression model implemented as part of the `scikit-learn` machine learning package in Python as a `RandomForestRegressor` function.

The random forest method is an ensemble learning method that can be used for classification, regression, and other tasks by constructing an ensemble of recursively defined decision trees at training time. Each tree uses a random portion of the original data as training and in the case of random forest regression tasks, the output of the method is the mean or average prediction of the individual trees [Watt, Borhani, and Katsaggelos \[2020\]](#). Random decision forests were first introduced by [Ho \[1995\]](#), who found that by combining forests of trees can produce a single high-performing model.

Furthermore, random forest algorithms also provide an estimate of the importance of each individual feature, also called *permutation importance*. To measure the feature's importance the values of each feature are permuted, generating new trees, and the *out-of-bag error* is calculated on the new perturbed data set. The *out-of-bag error* is used to validate random forest methods by averaging the error using predictions from samples that are not used in the training of a particular tree (*out-of-bag samples*). The importance score is calculated by averaging the difference between the out-of-bag error before and after the permutation over all trees. If a feature is important for the regression, the permutations will produce many errors, while if a feature is not important, the permutations will not have a large effect on the performance of the regression method.

We use the random forest regression model implementation from Python's `scikit-learn` package, in particular the `RandomForestRegressor` function. The `RandomForestRegressor` function has a number of input parameters including the following:

- *max\_depth*: maximum depth of the decision tree. The default value is `None`, which means that the tree is expanded until all leaves are pure or until all leaves contain less than the set minimum number of samples required to be on a leaf node.
- *max\_features*: maximum number of features that the model will consider when determining a split. The default value is `1.0` which translates to the number of features to be considered equal to the number of features seen during the training.
- *n\_estimators*: number of decision trees used in the training. The suggested default value is 100.
- *min\_samples\_leaf*: minimum number of samples required to be at a leaf node. The suggested default value is 2.
- *min\_samples\_split*: minimum number of samples required to split an internal node. The suggested default value is 1.

More information on other input parameters can be found in the `scikit-learn`'s `RandomForestRegressor` documentation `skl` [Accessed: 2023-09-19].

### 2.2.1. Performance Measures

To assess the performance of the random forest regression model, we use two statistical measures: (1) the *R-squared score* ( $R^2$ ), also called *coefficient of determination*; and (2) the *out-of-bag score*. In regression models, the  $R^2$  coefficient measures how well the regression predictions estimate the real data points. An  $R^2$  coefficient of determination equal to 1.0 signals that the predictions of the regression model perfectly fit the data. The *out-of-bag score* gives an estimate of the error rate of the training model for new data from the same distribution. The out-of-bag score is calculated by averaging only the trees for which a given data point prediction was not in the training data. This score is only available when `bootstrap=True`, which means that bootstrap samples are used when building the trees instead of using the whole data set for each tree. We enabled the out-of-bag score using the following command `oob_score=True`.

### 2.2.2. Features

Our primary control feature is the rate constant for the chemical reactions. We consider four rate constants ( $k$ ) of  $1 \cdot 10^{-9}$ ,  $1 \cdot 10^{-10}$ ,  $1 \cdot 10^{-11}$ ,  $1 \cdot 10^{-12}$  mol m<sup>-2</sup> s<sup>-1</sup>. We partition the fracture-based features for our into three categories: (1) topological, (2) geometric, and (3) hydrological. All of the features we consider are fracture-based.

**Topological features** To obtain and measure the topological features of the DFN, we adopt a graph-based representation as presented in Hyman et al. [2018]. Therein the fractures are represented as nodes in the graph and intersections between fractures are represented as edges. If two fractures intersect in the DFN, then there is an edge in the graph between the corresponding nodes. Formally, let  $\Omega = \{f_i\}$  for  $i = 1, \dots, N$  denote the entire network composed of  $N$  fractures and let  $\mathcal{E}_{i,j}$  be the set of intersections between fractures, i.e.,  $f_i \cap f_j \neq \emptyset \equiv \mathcal{E}_{i,j}$ . We define a graph  $G = (V, E)$  of node set  $V$  and edge set  $E$  using a mapping  $\phi$  defined in the following way. For every fracture  $f_i \in \{f_i\}$ , there is a node  $v \in V$ ,

$$\phi : f_i \rightarrow v_i. \quad (8)$$

Similarly, for every intersection in  $\mathcal{E}_{i,j}$ , there is edge  $e_{i,j} \in E$  that connects the corresponding nodes in  $V$

$$\phi : f_i \cap f_j \neq \emptyset \rightarrow e_{i,j} = (v_i, v_j). \quad (9)$$

We also include nodes representing the inflow and outflow boundaries  $G$  to account for the direction of flow. Every fracture that intersects the inlet plane  $\mathbf{x}_0$  is connected to the source node  $s$

$$\phi : f_i \cap \mathbf{x}_0 \neq \emptyset \rightarrow (s, v_i). \quad (10)$$

Likewise, every fracture that intersects the outlet plane  $\mathbf{x}_L$  is connected to the source node  $t$

$$\phi : f_i \cap \mathbf{x}_L \neq \emptyset \rightarrow (v_i, t). \quad (11)$$

Similar mappings have been used in the literature Hope, Davy, Maillot, Le Goc, and Hansen [2015], Andresen, Hansen, Le Goc, Davy, and Hope [2013], Hyman et al. [2017]. Note that the mapping  $\phi$  is an isomorphic bijection, which means that every subgraph in the graph corresponds to a unique subnetwork in the DFN. The graph is handled using NetworkX Hagberg, Schult, and Swart [2008] and all graph-based features are computed using built-in algorithms within NetworkX.

Figure 2 shows a graph representation of one DFN from our set of simulations, other networks exhibit the same behavior. We represent each DFN using a graph to characterize topological structure influences for the distribution of reactive transport within the network. In Figure 2 (a) fractures are colored by their remaining quartz volume at the end of the simulation and (b) fractures are partitioned by whether their effective Péclet number at the start of the simulation is diffusion dominated ( $Pe < 1$ ) or advection dominated ( $Pe \geq 1$ ). There is almost no quartz remaining in fractures that were initially advection-dominated - compare Fig. 2 (a) and (b). However, there remains a substantial amount of quartz in the fractures that were initially diffusion-dominated. Flow channelization, isolated regions of higher volumetric flow rates, is a commonly observed phenomenon in field and laboratory experiments as well as numerical simulations in fractured media Abelin, Birgersson, Moreno, Widén, Ågren, and Neretnieks [1991], Abelin, Neretnieks, Tunbrant, and Moreno [1985], de Dreuzy et al. [2012], Frampton and Cvetkovic [2011], Hyman [2020], Rasmuson and Neretnieks [1986]. This phenomenon is observed in Figure 2 (b) where advection-dominated pathways connecting inflow and outflow boundaries (blue triangle and red circles respectively) can be seen. These flow channels indicate the existence of primary sub-networks, also referred to as backbones, within the fracture network. To this end, we partition the network into disjoint primary and secondary sub-networks. Formally, let  $\Omega = \{f_i\}$  for  $i = 1, \dots, N$  denote the entire network composed of  $N$  fractures, then

$$\Omega = \Omega' \cup \Omega^* \quad \text{and} \quad \Omega' \cap \Omega^* = \emptyset, \quad (12)$$

where  $\Omega'$  and  $\Omega^*$  are the primary and secondary sub-networks. We define the secondary network to be comprised of all dead-end structures, i.e., dead-end fractures and cycles, and the primary sub-network is its complement, similar to the methods proposed in Doolaege, Davy, Hyman, and Darcel [2020] and Yoon et al. [2023]. Our partitioning definition is based solely on the network structure, specifically the topology/connectivity, and does not utilize any hydraulic, geometric, or flow information. To do so, we compute the current-flow through the network using Kirchhoff's laws with one unit of current is injected into the graph at the source node and one unit is extracted at the target, and every edge has unit resistance. Kirchhoff's law expresses that the sum of incoming currents at a node must be equal to the sum of outgoing currents. Defining the sign of incoming currents as positive and the sign of outgoing current as negative, then the law can be represented that the sum of the currents at each node is zero,

$$\sum_j^n I_{i,j} = 0 \quad \forall v_i \in V. \quad (13)$$

Once the current is determined on every edge, all edges with current less than machine precision ( $\epsilon = 10^{-16}$ ) are removed.

$$E' = \{e_{i,j}\} \text{ if } I_{i,j} > \epsilon. \quad (14)$$

Then any nodes that are no longer connected to the sub-network containing the source are target are removed.

$$V' = \{v_i\} \text{ if } |e_{i,\cdot}| > 0, \quad (15)$$



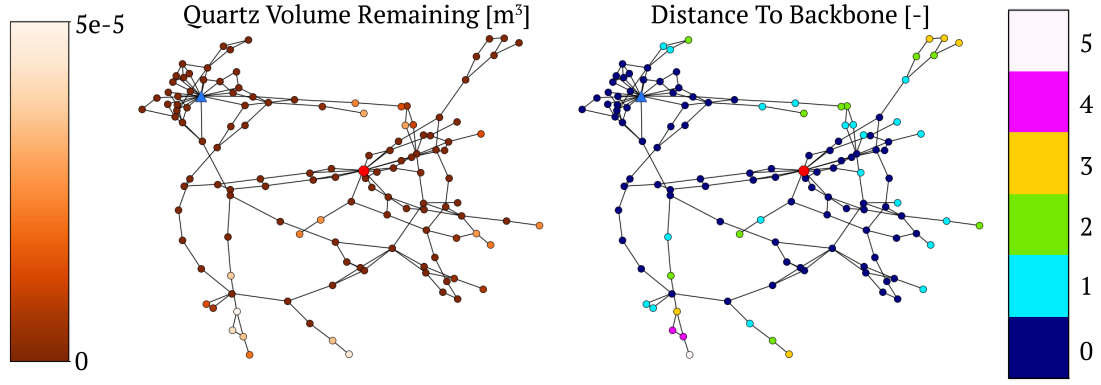


**Figure 2:** Graph representations based on the DFN shown above. (left) Nodes/fractures are colored by (left) quartz volume remaining (right) topological distance to the backbone. Distance to the backbone equal to 0 refers to a fracture on the backbone (primary sub-network membership).

where  $|e_{i,\cdot}|$  is the number of edges with an endpoint on the node  $v_i$ . Then our primary sub-graph is defined as

$$G' = (V', E'), \quad (16)$$

and the secondary its complement

$$G^* = G \setminus G'. \quad (17)$$

Recalling that the mapping  $\phi$  is a bijective isomorphism allows us to extract the primary and secondary sub-networks of the DFN

$$\phi^{-1} : G' \rightarrow \Omega' \quad \text{and} \quad \phi^{-1} : G^* \rightarrow \Omega^*. \quad (18)$$

1. *Node Degree:* The degree of a node  $v_i$  is the number of edges with one endpoint on the node  $v_i$ . It describes the number of intersections on the corresponding fracture. Formally,

$$\text{Degree}(v_i) = \sum_{j=1}^n A_{ij}, \quad (19)$$

where  $A_{i,j}$  is the adjacency matrix of the graph  $G$  in which the entry  $a_{i,j}$  is the number of edges in  $G$  with end points  $e_{i,j} = (v_i, v_j)$ . Nodes with a larger degree are well connected and ought to be a location of substantial transport and reactions.

2. *Degree Centrality:* Degree centrality is a normalized measure of the node degree defined above. For vertex  $i$ ,

$$\text{Degree centrality}(v_i) = \frac{1}{n-1} \sum_{j=1}^n A_{ij}. \quad (20)$$

High degree centrality indicates that a node is well connected and such nodes tend to be concentrated in the core of the network. Nodes with low degree centrality are often in the periphery or on branches that cannot conduct significant flow and transport. Physically, it describes the number of other fractures that intersect with a given fracture.

3. *Distance to Backbone:* If a fracture is on the backbone, then the distance to the backbone is 0. If the fracture is in the secondary sub-network, then the value is the shortest topological path from that fracture to one on the backbone. Formally,

$$\text{Distance to backbone}(v_i) = \begin{cases} 0, & \text{if } f_i = \Omega' \\ \min d(f_i, f_j) \forall f_j \in \Omega' & \text{if } f_i \neq \Omega' \end{cases} \quad (21)$$

where the topological distance metric  $d(u_i, u_j)$  counts the number of edges between the nodes  $u_i, u_j$ . In practice, we use an unweighted Dijkstra's method implemented in NetworkX for the search. Primary/secondary membership is a good indicator of the final quartz volume in each fracture – compare Fig. 2 (a) and (c). Almost all of the quartz has been dissolved out of the primary sub-network and there is a significant volume remaining in the secondary sub-network fractures. Beyond a Boolean of backbone membership, the distance to the backbone includes more information about the proximity of a fracture in the secondary sub-network to the backbone. Reactions in fractures that are farther away from the backbone tend to transport limited and therein remains more quartz.

4. *Betweenness Centrality*: The betweenness centrality Anthonisse [1971], Freeman [1977] of a node describes the extent to which a node can control communication on a network. Consider a path with the fewest possible edges (geodesic path), that connects a node  $u$  and a node  $v$  on a graph. In general, there may be more than one such paths, and with  $\sigma_{uv}$ , we denote the number of such geodesic paths. Furthermore, let  $\sigma_{uv}(i)$  denote the number of such paths that pass through node  $i$ . We then define, for node  $i$ ,

$$\text{Betweenness centrality} = \frac{1}{(n-1)(n-2)} \sum_{\substack{u,v=1 \\ u \neq i \neq v}}^n \frac{\sigma_{uv}(i)}{\sigma_{uv}}, \quad (22)$$

where the leading factor normalizes the quantity so that it can be compared across graphs of different sizes  $n$ . Many backbone nodes have high betweenness values; however, other paths through the network can show high values, since this feature considers *all* paths in the graphs, and not only those from source to target.

5. *Source-to-target Current Flow*: This is a type of centrality measure adopted from an electrical current model Brandes and Fleischer [2005]. The current flow assumes a given source and target. Imagine that one unit of current is injected into the network at the source, one unit is extracted at the target, and every edge has one unit of resistance. Then, the current flow centrality is given by the current passing through a given node. This can be described by Kirchhoff's laws, or in terms of the graph Laplacian matrix  $\mathbf{L} = \mathbf{D} - \mathbf{A}$ , where  $\mathbf{A}$  is the adjacency matrix for the graph and  $\mathbf{D}$  is a diagonal matrix specifying node degree:  $D_{ii} = \sum_j A_{ij}$ . We can define the current flow for node  $i$  as

$$\text{Current flow } (v_i) = \sum_{j=1}^n A_{ij} \left| (L_{is}^+ - L_{js}^+) - (L_{it}^+ - L_{jt}^+) \right|, \quad (23)$$

where  $\mathbf{L}^+$  is the Moore-Penrose pseudoinverse of  $\mathbf{L}$ ,  $s$  is the source node, and  $t$  is the target node.

The current flow centrality is often referred to as random-walk centrality Newman [2005], measuring how often a random walk from the source ( $s$ ) to the target ( $t$ ) passes through a node  $i$ . Unlike betweenness centrality, the current flow centrality considers only the paths from source to target, it's values are zero on any branch of the graph outside of the central core. Thus, we expect a correlation between high current flow values and nodes that have a large influence on the transport from source to target.

**Geometric Features** The following features are based on the fracture geometry. Recall that fractures are planar discs with the same initial aperture and radius. So, initially, they all have the same surface area and volume. However, if a fracture intersects with the domain boundary, its shape is modified to conform to the boundary. Therefore, there is variation in the following attributes.

1. *Surface area*: The surface area of the polygon representing the fracture plane. For a non-truncated fracture, the value is equal to  $\pi r^2$ .
2. *Total fracture volume*: The total volume of the fracture is the surface area, which varies between fractures, and the aperture, which is initially constant.

$$\text{Total fracture volume } n_i = V_i. \quad (24)$$

The total fracture volume determines the initial amount of quartz in each fracture, being the total volume multiplied by the initial volume fraction (80%). Because the total quartz volume is a constant scaled quantity of the total fracture volume, we only include the total fracture volume as a feature.

3. *Projected volume*: The projected volume of the fracture is the component of a fracture's volume-oriented parallel to the main flow direction (inlet to outlet plane). Assuming the flow is oriented along the  $x$ -axis, the projected volume is expressed as

$$\text{Projected volume} = V_i \sqrt{(\mathbf{O}_i)_y^2 + (\mathbf{O}_i)_z^2}, \quad (25)$$

where  $V_i$  is the volume of fracture  $i$  and  $\mathbf{O}_i$  is the unit vector normal to the fracture plane, called the orientation vector. Since the flow is oriented along the  $x$ -axis, the projected volume is expressed by the projection of  $\mathbf{O}_i$  onto the  $yz$ -plane. Fractures that are oriented along the main flow direction are more likely to carry a significant part of the flow, compared to the fractures oriented perpendicular to the normal flow direction.

4. *Intersection area*: The intersection area is the total length of intersections on a fracture multiplied by the initial aperture.

**Hydrological Features** The following are a set of hydrological features that are computed on a pipe-network representation of the DFN, cf. Karra, O'Malley, Hyman, Viswanathan, and Srinivasan [2018] for details about how the pipe/graph-network is obtained and the numerical simulations are performed. Steady pressure-driven flow is computed to obtain pressure and volumetric flow rates throughout the DFN. Obtaining these values is computationally inexpensive especially when compared to the high-fidelity reactive transport simulations.

1. *Volumetric Flow Rate*: We compute the volumetric flow rate of fluid passing through each fracture. Given the flow rates into and out of the fracture, we take a single value that is one-half the absolute value of total flow exchanged by a fracture with its neighbors,

$$Q(f_i) = \frac{1}{2} \sum_j^n |Q_{i,j}|. \quad (26)$$

The absolute value is necessary because of the sign dependence of flow into (positive) and outgoing (negative) and the  $1/2$  is to account for double counting.

2. *Péclet Number*: We compute the Péclet number of each fracture using the volumetric flow rate  $Q_i$ , fracture radius  $r_i$ , and surface area  $S_i$  and the diffusion coefficient  $D = 10^{-12} \text{ m}^2/\text{s}$

$$Pe(f_i) = \frac{Q_i r_i}{S_i D}. \quad (27)$$

Regions with a high Péclet tend to occur within the primary sub-network and reactions therein are kinetically limited, i.e., there is sufficient volumetric flow to flush away the aqueous silica, and once the quartz is fully dissolved in the primary sub-network, than a quasi-steady state is reached, and the overall apparent dissolution rate slows.

3. *Advective Damköhler Number*: The advective Damköhler number compares the reaction timescale to the convection. We compute it on a fracture basis, similar to the Péclet number. First, we convert the rate constant  $k$  [ $\text{mol m}^2/\text{s}$ ] used in simulations to a rate  $k'$  [ $\text{m/s}$ ] using the quartz molar volume ( $V_m = 22.6880 \cdot 10^{-6} \text{ m}^3/\text{mol}$ ,  $k' = kV_m$ ). Then our advective Damköhler number is defined as

$$Da_I(f_i) = \frac{k S_i}{Q_i}. \quad (28)$$

4. *Diffusive Damköhler Number*: Likewise, we compute the diffusive Damköhler which compares the reaction timescale to diffusion and is given as

$$Da_{II}(f_i) = \frac{k r_i}{D}. \quad (29)$$

In the following section, we discuss the feature importance analysis obtained from the random forest regression model, as well as the accuracy of the trained ML models.

### 3. Results

We used 800 generic networks for training and testing the ML random forest regression model. Each DFN was run with four reaction rate constants, ( $k$ ) of  $1 \cdot 10^{-9}$ ,  $1 \cdot 10^{-10}$ ,  $1 \cdot 10^{-11}$ ,  $1 \cdot 10^{-12}$  mol m<sup>-2</sup> s<sup>-1</sup>, equal to a total of 3256 networks. The DFNs consist of a set of fractures (on average 133 fractures per network) and each fracture is considered a sample and was used to train or test the random regression model. The total number of fractures in the data set is 446,129 fractures, and two-thirds (2/3) of the data were used for training the ML model (*training set*), while the rest of the data (1/3) were used for testing the model (*testing set*). We trained a regression model to predict the quartz volume that remains in a given fracture depending on three different attribute sets – using only topological, geometric, and hydrological features as described above, along with the rate constant which we consider a primary control feature. Our results show that having access to flow features enhances the accuracy of the quartz volume prediction, however, it is not significant.

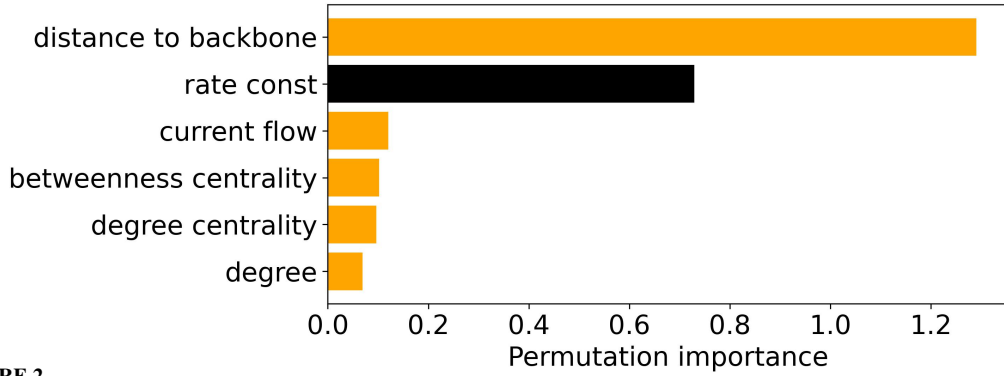
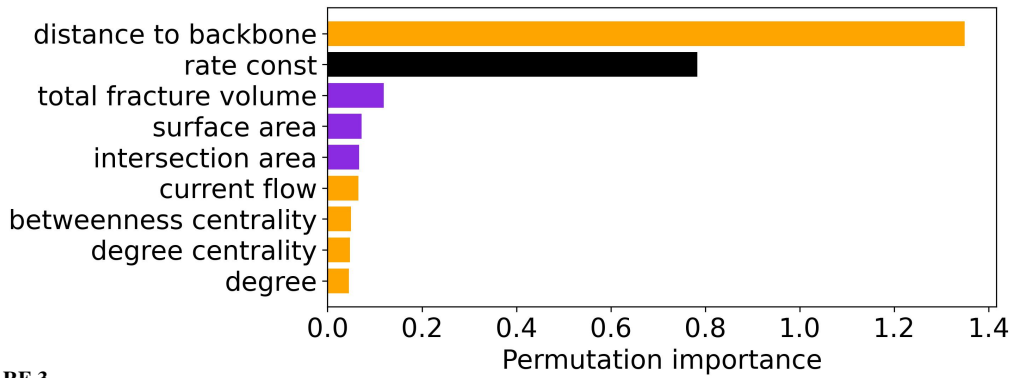
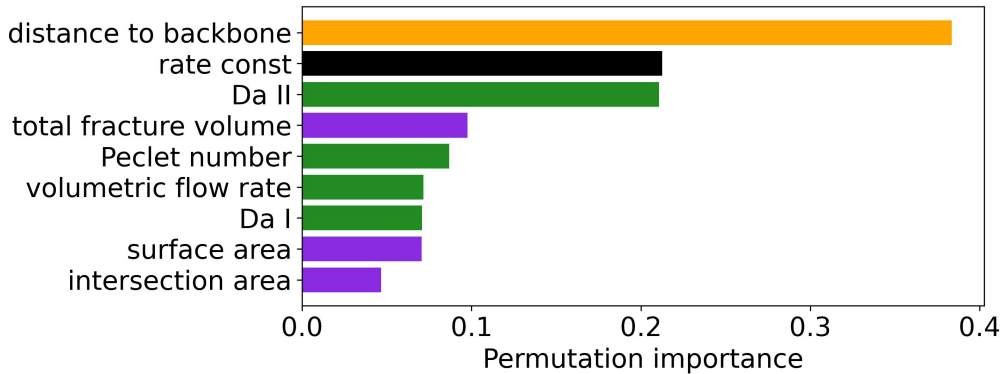
In the following subsection, we discuss the feature importance analysis, giving us insights into the significance of each feature in predicting the remaining quartz volume within a given fracture. This analysis shows an interplay between the feature categories and their correlations. Later, we show details on the performance of the following two types of random forest regression models: (1) including all rate constants and gradually adding more complexity regarding the feature categories. For this type, we generated the following three regression models: **RF-1** model using only topological features; **RF-2** model using topological and geometric features; **RF-3** model using topological, geometric, and hydrological features; (2) including one rate constant at a time while using all features, resulting in four regression models for each of the rate constants.

#### 3.1. Feature Importance

As mentioned previously the random forest regression model can be used to identify the importance of each individual feature for the performance of the trees. Figure 3 depicts the input feature importance analysis results for the three random forest regression models (RF-1, RF-2, and RF-3), with a gradually increasing number of features. Each model uses all values of the rate constant, shown in black. The topological features are displayed in orange, the geometrical features in purple, and the hydrological features in green.

The feature importance analysis is calculated by comparing the baseline model to the model obtained by permutating the feature column. As shown in Figure 3, the analysis confirms that the distance to the backbone and the rate constant are the two main quantities controlling the dissolution of quartz in the fractures for all regression models. This is not surprising since the distance to the backbone indicates how far a fracture is with respect to the backbone. The transport in fractures that are farther away from the backbone tend to be diffusion-dominated, thus therein remains more quartz. Contrary, when a given fracture is part or in the vicinity of the primary sub-network, the behavior in the fracture is advection-dominated, which leads to the complete depletion of quartz within the fractures. The rate constant is the second important feature for all trained regression models because it indicates the strength of dissolution in the fracture. There is a strong correlation between the distance to the backbone, reaction rate, and the quartz volume that remained in the system, since as the reaction rate increases also the dissolution penetrating deeper levels of the secondary fracture sub-network. This means that as higher the rate constant is, the more quartz will be flushed out from the secondary sub-network (taking into account that all quartz is dissolved from the primary sub-network). Conversely, when the rate constant is small, the reactive transport is reduced almost entirely to the primary sub-network.

As we increase the number of features from topological to topological and geometric, we can see that the total fracture volume, surface area and intersection area line up right after the first two topological features. When we add hydrological features, we observe that the diffusive Damköhler number ( $Da_{II}$ ) becomes almost as important as the rate constant, followed by the total fracture volume and other hydrological features. From the training results shown in Table 2, we know that the model accuracy does not improve drastically, when more features are included in the training; however, from the features importance analysis, we can confirm that they carry significant information for the flow and reactive transport of a fracture. Reactions during early simulation times are kinetically limited occurring mostly in the primary network. However, once all of the quartz in the primary network is dissolved, the secondary network becomes the location where all reactions are occurring. Flow in the secondary network is slow compared to the primary network (Péclet number  $< 1$ ) and reactions therein are transport limited rather than kinetically. Thus, reactions in the secondary network are a balance between diffusion and the reaction rate, which is diffusive Damköhler number measures. In other words,  $Da_{II}$  captures the integrated effects of the distance to the backbone, rate constant, and Péclet number into a

**RF-1****RF-2****RF-3**

**Figure 3:** Feature importance analysis for three regression models: RF-1 (topological features), RF-2 (topological and geometric features), and RF-3 (hydrological, topological and geometric features). The topological features are depicted in orange, the geometric features in purple, the topological features in green, and the reaction rate constant in black. The importance analysis for all models show that the distance to the backbone and the rate constant are the most important features in our study.

single variable which is then linked with late time dissolution effects and prediction of the remaining quartz in the system.

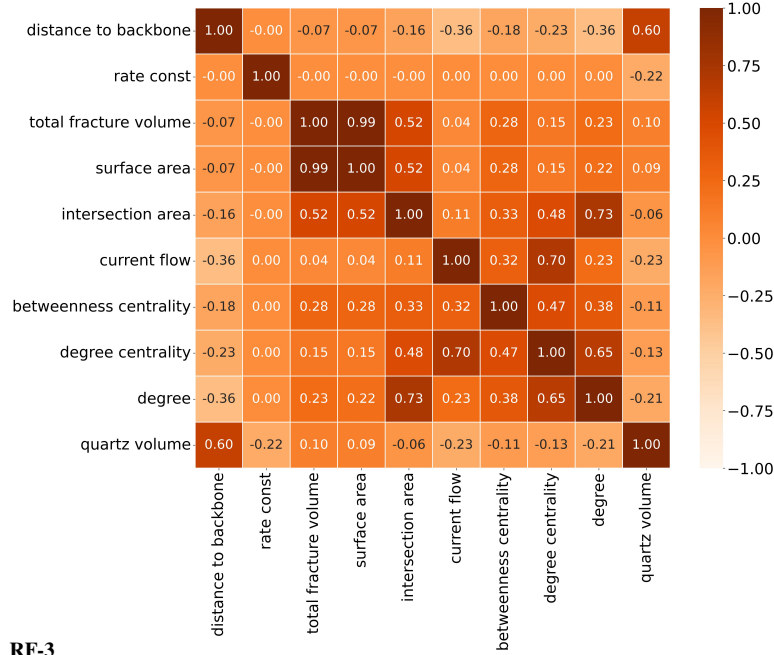
Figure 4 shows the correlations between input features (correlation matrix) in our regression model as a heat map. We omitted the correlation matrix for the RF-1 model since the topological features are depicted in RF-2 and RF-3. We reduced the number of features for each heat map to ten to improve the readability of the results.

The results for RF-2 show strong correlations between the following features: distance to the backbone and the quartz volume, total fracture volume and surface area (0.99), intersection area and degree (0.73), current flow and



## Learning the Factors Controlling Mineralization for GCS

### RF-2



### RF-3

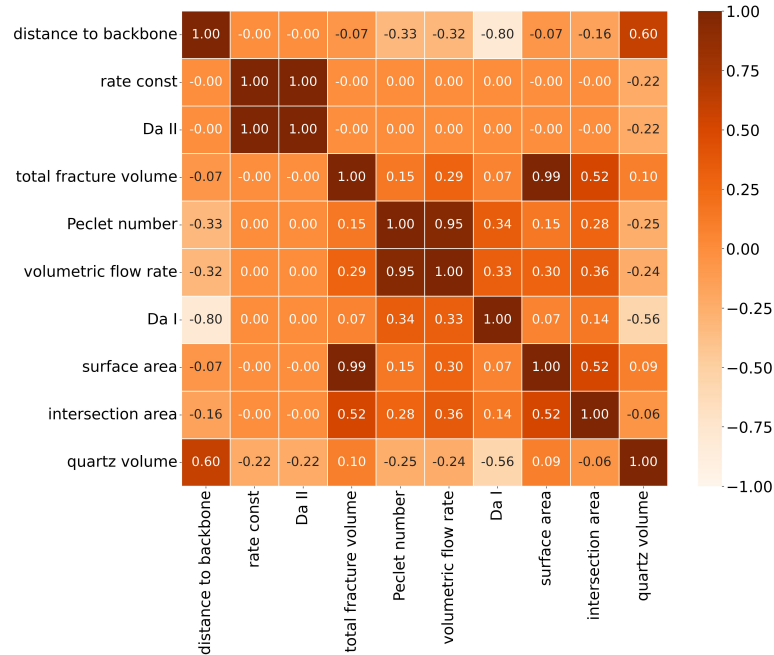


**Figure 4:** Correlation matrix of the model features displayed as a heat map for the remaining quartz volume and the first nine features used for the random forest regression training. The results for RF-2 show strong correlations between the following features: distance to the backbone and the quartz volume, total fracture volume and surface area, intersection area and degree, current flow, and degree centrality. When we add the hydrological features, some of the less significant topological features are not displayed. The RF-3 model shows a strong correlation between the aforementioned features and the following hydrological features:  $Da_{II}$  and rate constant, volumetric flow rate and Péclet number. We observe a strong inverse correlation between  $Da_I$  and the distance to the backbone, and  $Da_I$  and quartz volume. The RF-1 model is omitted for clarity.

RF Input Parameters	Grid Search	Base Model	Optimized Model
n_estimators	[10, 50, 100, 200, 300, 400, 500, 600, 700, 800, 900, 1000]	10	1000
max_depth	[None, 30, 60, 90]	None	30
max_features	[None, sqrt, log]	None	sqrt
min_samples_leaf	[2, 3, 4, 5]	2	2
min_samples_split	[1, 2, 3, 4, 5, 6, 7, 8]	1	2

**Table 1**

Hyperparameter ranges for the cross-validate grid-search and results. We show the default parameters used for the base model, as well as the optimized hyperparameters, resulting from the grid-search. To obtain these results, we use the RF-3 model, which contains all input features (topological, geometric, hydrological, and the reaction rate constant). Additionally, we set the following parameters for all regression models: `bootstrap=True`, and `oob_score=True`.

degree centrality (0.70). When we add the hydrological features, some of the less significant topological features are not displayed. The RF-3 model show strong correlation between the aforementioned features and the following hydrological features: diffusive Damköhler number ( $Da_{II}$ ) and rate constant (1.0), volumetric flow rate and Péclet number (0.95). We observe a strong inverse correlation between the advective Damköhler number ( $Da_I$ ) and the distance to the backbone (-0.8), and the advective Damköhler number ( $Da_I$ ) and the quartz volume (-0.56). This is expected since these variables are derived from one another, and it confirms that the regression models learn the correct behavior by being able to predict those strong correlations.

### 3.2. Regression Models

To implement the random forest regression model we used the `RandomForestRegressor` function from the `scikit-learn` module in Python. We performed an exhaustive cross-validated grid search over a number of parameter values using the `GridSearchCV` function. The optimized model was obtained after a grid-search through the following parameters: `n_estimators`, `max_depth`, `max_features`, `min_samples_leaf`, and `min_samples_split`. The ranges for each of these hyperparameters are given in Table 1. The input parameters used for the grid-search study include all the features: topological, geometric, hydrological, and the reaction rate constant (RF-3) as described in Section 2.2.2.

The time needed for the cross-validated grid search was about 20 hours on a CPU machine. The time to train the R3 base model is approximately 20 seconds, while the optimized model needs around 7.5 minutes. This is mainly due to the number of estimators used for the optimized model. Even though the optimized model takes almost 22 times slower, the model is more robust and prone to overfitting.

Table 2 shows a performance comparison between the base model (using the default parameters for the `RandomForestRegressor` function) and the optimized model using the  $R^2$  value obtained during training and testing, and the out-of-bag score.

The performance measured in Table 2 shows that the remaining quartz volume is hard to predict. When using only the topological features (RF-1 model), the random forest regression models (base and optimized) perform poorly, indicating that the topological features do not carry enough information to train the model. Adding geometric features enhances significantly the performance of both models, the base and the optimized. The  $R^2$  train values of the optimized model actually decrease in comparison to the base model; however, we expect that is due to overfitting of the base model. Including hydrological features (RF-3 model) only slightly increases the accuracy of the models, pointing to the complexity of the DFN system exhibiting dissolution.

The overall accuracy of the training for the base and the optimized model is good, however, during testing the coefficient of determination ( $R^2$  value) drops significantly. This is very clear for the RF-1 base model, where only topological input features are used. The train  $R^2$  is 0.9544, while during testing the model's test  $R^2$  value is only 0.7080, which implies that the random forest regression models overfit during training and show higher accuracy in training while under-performing during testing. The optimized models overfit less and perform slightly better than the base model. The small difference between the test  $R^2$  values of the base and the optimized model suggests that performing a grid

Model	R2 Values		OOB Score
	Train	Test	
Base RF-1	0.9410	0.6883	0.6256
Optimized RF-1	0.8864	0.7195	0.7179
Base RF-2	0.9672	0.8193	0.7658
Optimized RF-2	0.9506	0.8397	0.8356
Base RF-3	0.9701	0.8343	0.7845
Optimized RF-3	0.9499	0.8509	0.8474

**Table 2**

Performance measures of the random forest regression models. Comparison between the base regression model, using the default parameter values, and the optimized model, obtained from an exhaustive cross-validated grid search. These random forest models use all rate constants, while the number of input features is increased gradually with each model. The optimized model performs better than the base model. The out-of-bag score confirms that the optimized model is more robust.

search and tuning the model parameters, even though important, it might not improve the accuracy of the training significantly. This strongly depends on the data set and the problem at hand.

The out-of-bag score of the optimized model is eight to nine points larger than the one of the base model. This confirms that the optimized model is more prone to overfitting and is more robust.

### 3.2.1. Regression Models Using All Rate Constants

Training the regression model on all rate constants allows for comparison between different feature categories. Figure 5 shows the train and test results for the RF-1, RF-2, and RF-3 models. We see that using only the topological features is not sufficient to obtain a good regression model. The RF-1 test results are scattered and the model is not able to predict the correct target quartz values. By adding the geometric features (RF-2 model), we observe much better predictions of the remaining quartz volume. However, the random forest regression model still has difficulties predicting the quartz volume, especially when the quartz is either fully depleted or clogs the fracture (normalized quartz volume close to 0 or 1) in advection- or diffusion-dominated regions, respectively. We trained a third model (RF-3) that includes the hydrological features, which performs slightly better than the RF-2 model; however, the improvement is not significant.

### 3.2.2. Regression Models Using A Single Rate Constant

In order to have a better grasp on why training a regression model using all rate constants does not deliver a very accurate prediction for the quartz volume left in each fracture, we train four more random forest regression models using all input features and one rate constant at a time. The coefficient of determination (R2 value) during training and testing is depicted in Figure 6. One can see that the random forest regression model has difficulties predicting the remaining quartz volume for large rate constants, (k) of  $1 \cdot 10^{-9}$  and  $1 \cdot 10^{-10}$  mol m<sup>-2</sup> s<sup>-1</sup>, while for small rate constants, (k) of  $1 \cdot 10^{-11}$  and  $1 \cdot 10^{-12}$  mol m<sup>-2</sup> s<sup>-1</sup>, the model performs significantly better. When the rate constant is large, we expect more rapid quartz dissolution as fresh water is introduced to the system. This results in advection-dominated flow and quartz depletion in the backbone of the DFN, leading to shorter reactive transport simulation times since the quasi-steady state is reached in less time. It might seem a bit counter-intuitive, but for large rate constants the quartz volume in the system will be either flushed out completely from the fracture (mostly in a close proximity to the backbone, advection-dominated flow), or it will be clogging the fractures to a high extend (mostly in the secondary sub-network, diffusion-dominated flow), leading to sharp interfaces between the primary and the secondary sub-networks. This effect can be seen in Figure 6(a) and (b), where most of the samples are located either in the lower left or in the upper right corners. The figures seem to have fewer data samples, but this is not the case, the data points are simply overlapping in the aforementioned regions. This makes predicting the remaining quartz volume for a single fracture much harder for the regression model since the distance to the backbone feature will carry less significant information. Reaching a quasi-steady state for simulations with lower reaction rates, (k) of  $1 \cdot 10^{-11}$  and  $1 \cdot 10^{-12}$  mol m<sup>-2</sup> s<sup>-1</sup>, takes longer times since the reactions within fractures are slower. For those systems, we observe much smoother interfaces between the quartz-filled and quartz-depleted regions. This allows a smoother transition between these regions and more variability in the distance to the backbone feature, making the prediction of the remaining quartz volume an

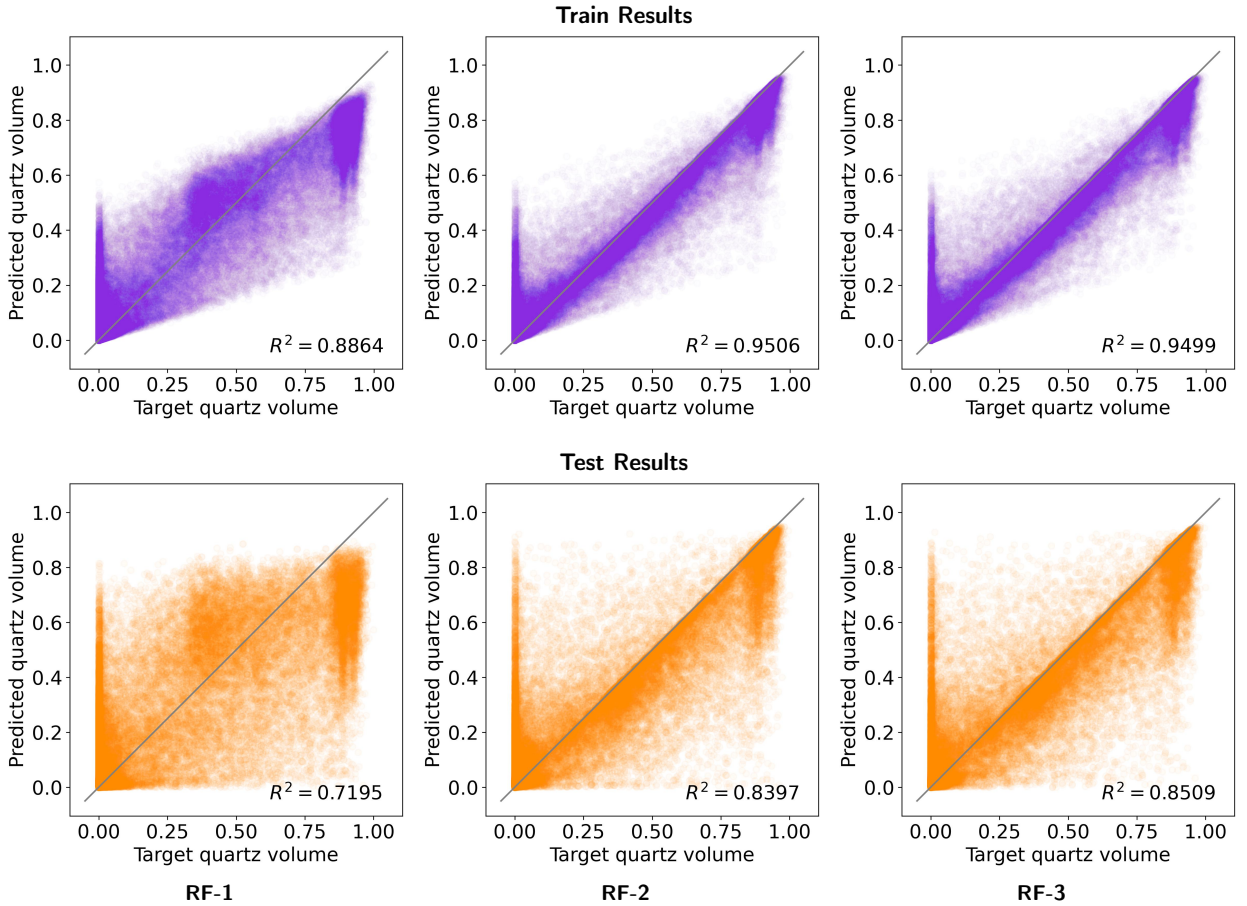


**Figure 5:** Random forest train (purple) and test (orange) predictions for the following models: RF-1 (topological features), RF-2 (topological and geometric features), and RF-3 (hydrological, topological, and geometric features). The RF-1 model does not include enough input parameters to predict correctly the remaining quartz volume in a given fracture. RF-2 shows tighter predictions; however, it still fails to predict the quartz volume for fractures that are either fully depleted or clogged (values close to 0 or 1, respectively). RF-3 gives slightly better predictions (see the  $R^2$  value); however, the improvement is not significant.

easier task. This is displayed in Figure 6(c) and (d), where the data samples are almost equally distributed in the range of quartz volume. In this case, the regression model predicts the remaining quartz volume with higher accuracy.

#### 4. Discussion and Conclusions

We have provided a set of numerical simulations along with random forest regression models to characterize the interplay of the network geostructure and geochemical reactions in fractured media. We generated a set of generic three-dimensional fracture networks composed of a single families of mono-disperse disc-shaped fractures. We simulated flow and reactive transport using four reaction rate constants, ( $k$ ) of  $1 \cdot 10^{-9}$ ,  $1 \cdot 10^{-10}$ ,  $1 \cdot 10^{-11}$  and  $1 \cdot 10^{-12}$  mol m $^{-2}$  s $^{-1}$ , to determine the important features that control mineralization in the form of dissolution. Prior to the simulation, the fractures are filled with quartz that dissolves gradually during the simulations until a quasi-steady state is reached. The DFN topology and the reaction rate control the amounts of quartz that remain in each fracture, which strongly differs within a fracture network. In order to understand better what causes these discrepancies, we combine DFN graph representation and machine learning techniques, in particular random forest regression models. We constructed two types of regression models: (1) using all rate constants while varying the number of feature categories (topological, geometric, and hydrological); and (2) using all available features and training the model only on one reaction rate at a time.

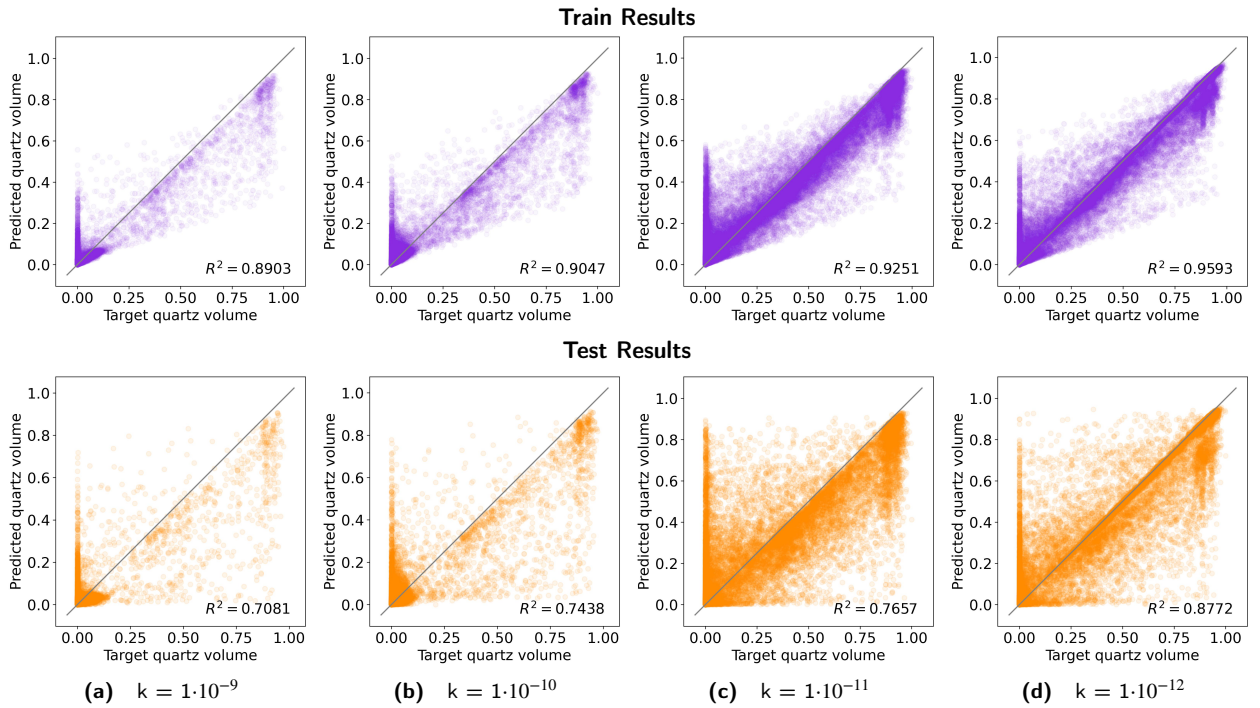


**Figure 6:** Random forest train and test predictions for each of the rate constants using all features (geometrical, topological, and hydrological). Each column depicts the results for a different rate constant. The regression model can predict the remaining quartz volume with higher accuracy for lower rate constants. The reaction rate constant is in  $[\text{mol m}^{-2} \text{s}^{-1}]$  units and each train/test model has an equal number of data samples.

The first type of ML model assessed the input feature importance for each of the models. The results showed that building a regression model to predict the remaining quartz volume for all reaction rate constants is a difficult endeavor. We can conclude that including topological and geometric features is instrumental in building a useful regression model predicting the remaining quartz volume in a quasi-steady state. Including the hydrological features are the least important ones since they only slightly improve the accuracy of the regression models. The most important features controlling the quartz dissolution are the rate constant and the distance to the backbone (primary sub-network), which can be easily explained since they control the flow channelization and the strength of the chemical reaction, respectively. The second type of ML model showed how the rate constant controls the dissolution in the DFN. The random forest regression model is able to predict the remaining quartz volume much better for low reaction rates in comparison to high reaction rates. This is due to smoother interfaces between the quartz-filled and quartz-depleted regions in the simulations using low rate constants, allowing for more variability in the quartz volume with respect to the distance to the backbone, which helps to build a better model.

In conclusion, we would like to summarize our findings:

- The reaction rate constant and the distance to the backbone are the two most important features for predicting the remaining quartz volume in a single fracture.
- The model has a hard time predicting the quartz volume remaining in a fracture using only topological features. However, adding geometric features improves the predictions significantly. Interestingly, including the hydrological features as well only slightly improves the regression model predictions. This indicates that each of these features sets contributes to the predictions in meaningful ways. In all models the distance to the backbone (a topological feature) was the most useful for prediction. This feature thereby provides a foundation for the other properties to refine upon.



- We performed an extensive cross-validated grid search. The optimized model delivers slightly better results compared to the base model. Even though the optimized model is much slower than the base model (approx. 22 times), it is more robust and prone to overfitting.
- High reaction rates, ( $k$ ) of  $1 \cdot 10^{-9}$  and  $1 \cdot 10^{-10}$   $\text{mol m}^{-2} \text{s}^{-1}$ , result in sharper interfaces between the quartz-filled and quartz-depleted fractures within a DFN while lower reaction rates, ( $k$ ) of  $1 \cdot 10^{-11}$  and  $1 \cdot 10^{-12}$   $\text{mol m}^{-2} \text{s}^{-1}$ , lead to smoother interfaces of quartz volume between the quartz-filled and quartz-depleted fractures within a DFN. In the former the backbone is completely depleted, while the fractures in the secondary sub-network are still filled with quartz. These reactive transport simulations take a shorter time to reach a quasi-steady state. The distance to the backbone, which we observe to be one of the most important features predicting the remaining quartz volume, becomes less significant as the quartz volume associated with it is either 0 or close to 1, as there is almost no variability in the overall network. In the case of the lower reaction rates, the simulation takes longer times to reach a quasi-steady state and the freshwater can penetrate deeper into the secondary network and dissolve larger amounts of the quartz in these fractures. In these cases, the distance to the backbone and the quartz volume associated with a specific fracture carries more variability and as such serves as a stronger predictor of the quartz volume compared to the same feature when high reaction rates are used. The occurrence of sharp interfaces could become more important if precipitation is considered as this could lead to system clogging.

As is slowly becoming better understood, our results reiterate that network connectivity is at the top of the hierarchy in determining flow and transport properties in fractured media. A primary contribution of this work is characterizing how that hierarchy influences reactions in fractured media as well. To this end, we observe the dynamic reactions in the system exhibit a strong interplay with the topology, geometry, and hydrology of the network. In summation, the complex structure of the fracture network determines the flow field and subsequent, which is then dynamically modified by the reactions. In terms of implications, our work indicates that a critical step in improving predictive capabilities of reactive in fractured media remains improving our ability to characterize fracture networks. However, it is currently unknown how the inclusion of precipitation which could lead to blocking would influence these results. It is feasible that the feedback loop of precipitation leading to lowering permeability could alter the importance of our determined features. Thus, the next step in this line of research is two fold. First, we need to characterize how changing fracture network properties influences our predictive capabilities as well as feature importance. Second, a gradual increase in chemical complexity is required to take these insights into the field. Both of these avenues warrant further exploration and detailed research.

## Acknowledgements

JDH, MRS, and HSV thank the Department of Energy (DOE) Basic Energy Sciences program (LANLE3W1) for support. JDH, MRS, and HSV also gratefully acknowledge support from the LANL LDRD program office Grant Number #20220019DR. AP acknowledges the Center for Non-Linear Studies at Los Alamos National Laboratory. Research was supported as part of the Center on Geo-process in Mineral Carbon Storage, an Energy Frontier Research Center funded by the U.S. Department of Energy (DOE), Office of Science, Basic Energy Sciences (BES), under Award #DE-SC0023429. Los Alamos National Laboratory is operated by Triad National Security, LLC, for the National Nuclear Security Administration of U.S. Department of Energy (Contract No. 89233218CNA000001). Assigned LA-UR-23-33803.

## References

- Curt M White, Brian R Strazisar, Evan J Granite, James S Hoffman, and Henry W Pennline. Separation and capture of  $\text{CO}_2$  from large stationary sources and sequestration in geological formations—coalbeds and deep saline aquifers. *Journal of the Air & Waste Management Association*, 53(6):645–715, 2003.
- Irina Gaus. Role and impact of  $\text{CO}_2$ –rock interactions during  $\text{CO}_2$  storage in sedimentary rocks. *International journal of greenhouse gas control*, 4(1):73–89, 2010.
- Hongbo Shao, Jessica R Ray, and Young-Shin Jun. Dissolution and precipitation of clay minerals under geologic  $\text{CO}_2$  sequestration conditions:  $\text{CO}_2$ -brine-phlogopite interactions. *Environmental science & technology*, 44(15):5999–6005, 2010.
- Kate Maher, Carl I Steefel, Art F White, and Dave A Stonestrom. The role of reaction affinity and secondary minerals in regulating chemical weathering rates at the santa cruz soil chronosequence, california. *Geochimica et Cosmochimica Acta*, 73(10):2804–2831, 2009.
- Joel Moore, Peter C Lichtner, Art F White, and Susan L Brantley. Using a reactive transport model to elucidate differences between laboratory and field dissolution rates in regolith. *Geochimica et Cosmochimica Acta*, 93:235–261, 2012.

- Alexis Navarre-Sitchler, Carl I. Steefel, Peter B. Sak, and Susan L. Brantley. A reactive-transport model for weathering rind formation on basalt. *Geochimica et Cosmochimica Acta*, 75(23):7644–7667, 2011. ISSN 00167037. doi: 10.1016/j.gca.2011.09.033.
- Art F. White, Marjorie S. Schulz, Davison V. Vivit, Alex E. Blum, David A. Stonestrom, and Suzanne P. Anderson. Chemical weathering of a marine terrace chronosequence, Santa Cruz, California I: Interpreting rates and controls based on soil concentration-depth profiles. *Geochimica et Cosmochimica Acta*, 72(1):36–68, 2008. ISSN 00167037. doi: 10.1016/j.gca.2007.08.029.
- J. D. Hyman and J. Jiménez-Martínez. Dispersion and mixing in three-dimensional discrete fracture networks: Nonlinear interplay between structural and hydraulic heterogeneity. *Water Resources Research*, 54(5):3243–3258, 2018. doi: 10.1029/2018WR022585.
- J. D. Hyman, M. Dentz, A. Hagberg, and P. Kang. Emergence of stable laws for first passage times in three-dimensional random fracture networks. *Phys. Rev. Lett.*, 123(24):248501, 2019a.
- J. D. Hyman, Joaquin Jimenez-Martinez, Carl W Gable, Philip H Stauffer, and Rajesh J Pawar. Characterizing the impact of fractured caprock heterogeneity on supercritical CO<sub>2</sub> injection. *Transp. Porous Media*, 131(3):935–955, 2020.
- Julien Maillot, Philippe Davy, Romain Le Goc, Caroline Darcel, and Jean-Raynald De Dreuzy. Connectivity, permeability, and channeling in randomly distributed and kinematically defined discrete fracture network models. *Water Resour. Res.*, 52(11):8526–8545, 2016.
- P. Kang, J. D. Hyman, W. S. Han, and M. Dentz. Anomalous transport in three-dimensional discrete fracture networks: Interplay between aperture heterogeneity and particle injection modes. *Water Resour. Res.*, 2020.
- Scott Painter, Vladimir Cvetkovic, and Jan-Olof Selroos. Power-law velocity distributions in fracture networks: Numerical evidence and implications for tracer transport. *Geophys. Res. Lett.*, 29(14), 2002.
- S.P. Neuman. Trends, prospects and challenges in quantifying flow and transport through fractured rocks. *Hydrogeol. J.*, 13(1):124–147, 2005.
- T. Sherman, J. D. Hyman, D. Bolster, N. Makedonska, and G. Srinivasan. Characterizing the impact of particle behavior at fracture intersections in three-dimensional discrete fracture networks. *Phys. Rev. E*, 2018.
- Matthew Ryan Sweeney and JD Hyman. Stress effects on flow and transport in three-dimensional fracture networks. *Journal of Geophysical Research: Solid Earth*, 125(8):e2020JB019754, 2020.
- Matthew R Sweeney, Jeffrey D Hyman, Daniel O’Malley, Javier E Santos, J William Carey, Philip H Stauffer, and Hari S Viswanathan. Characterizing the impacts of multi-scale heterogeneity on solute transport in fracture networks. *arXiv preprint arXiv:2306.00773*, 2023.
- Seonkyoo Yoon, Jeffrey D Hyman, Weon Shik Han, and Peter K Kang. Effects of dead-end fractures on non-fickian transport in three-dimensional discrete fracture networks. *Journal of Geophysical Research: Solid Earth*, page e2023JB026648, 2023.
- Elizabeth Andrews and Alexis Navarre-Sitchler. Temporal and spatial heterogeneity of mineral dissolution rates in fractured media. *Geochimica et Cosmochimica Acta*, 312:124–138, 2021.
- Adam L Atchley, Reed M Maxwell, and Alexis K Navarre-Sitchler. Using streamlines to simulate stochastic reactive transport in heterogeneous aquifers: Kinetic metal release and transport in CO<sub>2</sub> impacted drinking water aquifers. *Advances in Water Resources*, 52:93–106, 2013.
- James J Beisman, Reed M Maxwell, Alexis K Navarre-Sitchler, Carl I Steefel, and Sergi Molins. Parcrunchflow: an efficient, parallel reactive transport simulation tool for physically and chemically heterogeneous saturated subsurface environments. *Computational Geosciences*, 19(2): 403–422, 2015.
- Heewon Jung and Alexis Navarre-Sitchler. Physical heterogeneity control on effective mineral dissolution rates. *Geochimica et cosmochimica Acta*, 227:246–263, 2018a.
- EM Andrews, JD Hyman, MR Sweeney, S Karra, JD Moulton, and A Navarre-Sitchler. Fracture intensity impacts on reaction front propagation and mineral weathering in three-dimensional fractured media. *Water Resources Research*, 59(2):e2022WR032121, 2023.
- Brian Berkowitz and Harvey Scher. Anomalous transport in random fracture networks. *Phys. Rev. Lett.*, 79(20):4038, 1997.
- M. W Becker and A. M Shapiro. Tracer transport in fractured crystalline rock: Evidence of nondiffusive breakthrough tailing. *Water Resour. Res.*, 36(7):1677–1686, 2000.
- Yaniv Edery, Sebastian Geiger, and Brian Berkowitz. Structural controls on anomalous transport in fractured porous rock. *Water Resour. Res.*, 52(7):5634–5643, 2016.
- Sebastian Geiger, A Cortis, and JT Birkholzer. Upscaling solute transport in naturally fractured porous media with the continuous time random walk method. *Water Resour. Res.*, 46(12), 2010.
- Roy Haggerty, Sean W Fleming, Lucy C Meigs, and Sean A McKenna. Tracer tests in a fractured dolomite: 2. analysis of mass transfer in single-well injection-withdrawal tests. *Water Resour. Res.*, 37(5):1129–1142, 2001.
- O Huseby, J-F Thovert, and PM Adler. Dispersion in three-dimensional fracture networks. *Phys. Fluids*, 13(3):594–615, 2001.
- Jeffrey D. Hyman, Harihar Rajaram, Shriram Srinivasan, Natalia Makedonska, Satish Karra, Hari Viswanathan, and Gowri Srinivasan. Matrix diffusion in fractured media: New insights into power law scaling of breakthrough curves. *Geophys. Res. Lett.*, 46(23):13785–13795, 2019b. doi: 10.1029/2019GL085454.
- Heewon Jung and Alexis Navarre-Sitchler. Scale effect on the time dependence of mineral dissolution rates in physically heterogeneous porous media. *Geochimica et Cosmochimica Acta*, 234:70–83, 2018b.
- Sachin Pandey and Harihar Rajaram. Modeling the influence of preferential flow on the spatial variability and time-dependence of mineral weathering rates. *Water Resources Research*, 52(12):9344–9366, 2016.
- Lucy C. Meigs and Richard L. Beauheim. Tracer tests in a fractured dolomite: 1. experimental design and observed tracer recoveries. *Water Resour. Res.*, 37(5):1113–1128, may 2001. doi: 10.1029/2000wr900335. URL <https://doi.org/10.1029/2000wr900335>.
- Hang Wen and Li Li. An upscaled rate law for mineral dissolution in heterogeneous media: The role of time and length scales. *Geochimica et Cosmochimica Acta*, 235:1–20, 2018. ISSN 0016-7037.
- Hang Deng, Sergi Molins, David Trebotich, Carl Steefel, and Donald DePaolo. Pore-scale numerical investigation of the impacts of surface roughness: Upscaling of reaction rates in rough fractures. *Geochimica et Cosmochimica Acta*, 239:374–389, 2018. ISSN 00167037. doi: 10.1016/j.gca.2018.08.005. URL <https://doi.org/10.1016/j.gca.2018.08.005>.
- Jianwei Feng, Xu Zhang, Peng Luo, Xizhe Li, and He Du. Mineral filling pattern in complex fracture system of carbonate reservoirs: implications from geochemical modeling of water-rock interaction. *Geofluids*, 2019:1–19, 2019.

- Marina I. Lebedeva and Susan L. Brantley. Weathering and erosion of fractured bedrock systems. *Earth Surface Processes and Landforms*, 42(13): 2090–2108, 2017. ISSN 10969837. doi: 10.1002/esp.4177.
- Trevor A Jones and Russell L Detwiler. Mineral precipitation in fractures: Using the level-set method to quantify the role of mineral heterogeneity on transport properties. *Water Resources Research*, 55(5):4186–4206, 2019.
- Sergi Molins, David Trebotich, Bhavna Arora, Carl I. Steefel, and Hang Deng. Multi-scale Model of Reactive Transport in Fractured Media: Diffusion Limitations on Rates. *Transport in Porous Media*, 128(2):701–721, 2019. ISSN 15731634. doi: 10.1007/s11242-019-01266-2.
- Catherine Noiriél, Nicolas Seigneur, Pierre Le Guern, and Vincent Lagneau. Geometry and mineral heterogeneity controls on precipitation in fractures: An x-ray micro-tomography and reactive transport modeling study. *Advances in Water Resources*, 152:103916, 2021.
- Carl I. Steefel and Peter C. Lichtner. Multicomponent reactive transport in discrete fractures: I. Controls on reaction front geometry. *Journal of Hydrology*, 209(1-4):186–199, 1998. ISSN 00221694. doi: 10.1016/S0022-1694(98)00146-2.
- Carl I Steefel and Antonio C Lasaga. A coupled model for transport of multiple chemical species and kinetic precipitation/dissolution reactions with application to reactive flow in single phase hydrothermal systems. *American Journal of science*, 294(5):529–592, 1994.
- Carl I Steefel and Mengsu Hu. Reactive transport modeling of mineral precipitation and carbon trapping in discrete fracture networks. *Water Resources Research*, 58(9):e2022WR032321, 2022.
- Jeffrey D Hyman, Alexis Navarre-Stichler, Elizabeth Andrews, Matthew R Sweeney, Satish Karra, J William Carey, and Hari S Viswanathan. A geo-structurally based correction factor for apparent dissolution rates in fractured media. *Geophysical Research Letters*, 49(15):e2022GL099513, 2022a.
- Elizabeth Santiago, Jorge X Velasco-Hernández, and Manuel Romero-Salcedo. A methodology for the characterization of flow conductivity through the identification of communities in samples of fractured rocks. *Expert Systems with Applications*, 41(3):811–820, 2014.
- JN Goetz, Alexander Brenning, Helene Petschko, and Philip Leopold. Evaluating machine learning and statistical prediction techniques for landslide susceptibility modeling. *Computers & geosciences*, 81:1–11, 2015.
- Manuel Valera, Zhengyang Guo, Priscilla Kelly, Sean Matz, Vito Adrian Cantu, Allon G. Percus, Jeffrey D. Hyman, Gowri Srinivasan, and Hari S. Viswanathan. Machine learning for graph-based representations of three-dimensional discrete fracture networks. *Computat. Geosci.*, Jan 2018a. ISSN 1573-1499. doi: 10.1007/s10596-018-9720-1. URL <https://doi.org/10.1007/s10596-018-9720-1>.
- Shriram Srinivasan, Satish Karra, Jeffrey Hyman, Hari Viswanathan, and Gowri Srinivasan. Model reduction for fractured porous media: a machine learning approach for identifying main flow pathways. *Computational Geosciences*, 23:617–629, 2019.
- H. S. Viswanathan, Hyman J.D., S. Karra, D. O'Malley, S. Srinivasan, A. Hagberg, and G. Srinivasan. Advancing graph-based algorithms for predicting flow and transport in fractured rock. *Water Resour. Res.*, 2018.
- Velimir V Vesselinov, Maruti Kumar Mudunuru, Satish Karra, Dan O'Malley, and Boian S Alexandrov. Unsupervised machine learning based on non-negative tensor factorization for analyzing reactive-mixing. *Journal of Computational Physics*, 395:85–104, 2019.
- Bulbul Ahmmed, Maruti Kumar Mudunuru, Satish Karra, Scott C James, and Velimir V Vesselinov. A comparative study of machine learning models for predicting the state of reactive mixing. *Journal of Computational Physics*, 432:110147, 2021.
- Min Liu, Beomjin Kwon, and Peter K Kang. Machine learning to predict effective reaction rates in 3d porous media from pore structural features. *Scientific reports*, 12(1):5486, 2022.
- Daniel O'Malley, Satish Karra, JD Hyman, Hari Selvi Viswanathan, and Gowri Srinivasan. Efficient monte carlo with graph-based subsurface flow and transport models. *Water Resources Research*, 54(5):3758–3766, 2018.
- Philippe Davy, Romain Le Goc, and Caroline Darcel. A model of fracture nucleation, growth and arrest, and consequences for fracture density and scaling. *J. Geophys. Res.-Sol. Ea.*, 118(4):1393–1407, 2013.
- P. Davy, R. Le Goc, C. Darcel, O. Bour, J. R. de Dreuzy, and R. Munier. A likely universal model of fracture scaling and its consequence for crustal hydromechanics. *Journal of Geophysical Research: Solid Earth*, 115(B10), 2010. doi: 10.1029/2009JB007043.
- J.-R de Dreuzy, C Darcel, P Davy, and O Bour. Influence of spatial correlation of fracture centers on the permeability of two-dimensional fracture networks following a power law length distribution. *Water Resour. Res.*, 40(1), 2004.
- J.-R. de Dreuzy, Y. Méheust, and G. Pichot. Influence of fracture scale heterogeneity on the flow properties of three-dimensional discrete fracture networks. *J. Geophys. Res.-Sol. Ea.*, 117(B11), 2012.
- J Erhel, J-R de Dreuzy, and B Poirriez. Flow simulation in three-dimensional discrete fracture networks. *SIAM J. Sci. Comput.*, 31(4):2688–2705, 2009.
- J. D. Hyman, C. W. Gable, S. L. Painter, and N. Makedonska. Conforming Delaunay triangulation of stochastically generated three dimensional discrete fracture networks: A feature rejection algorithm for meshing strategy. *SIAM J. Sci. Comput.*, 36(4):A1871–A1894, 2014.
- Jeffrey D Hyman, Satish Karra, Nataliia Makedonska, Carl W Gable, Scott L Painter, and Hari S Viswanathan. dfnWorks: A discrete fracture network framework for modeling subsurface flow and transport. *Comput. Geosci.*, 84:10–19, 2015.
- Bernd Flemisch, Alessio Fumagalli, and Anna Scotti. *A Review of the XFEM-Based Approximation of Flow in Fractured Porous Media*, pages 47–76. Springer International Publishing, Cham, 2016. doi: 10.1007/978-3-319-41246-7-3.
- Shahid Manzoor, Michael G Edwards, Ali H Dogru, and Tareq M Al-Shaalan. Interior boundary-aligned unstructured grid generation and cell-centered versus vertex-centered cvd-mpfa performance. *Computational Geosciences*, 22(1):195–230, 2018.
- Jeffrey D Hyman, Matthew R Sweeney, Carl W Gable, Daniil Svyatsky, Konstantin Lipnikov, and J David Moulton. Flow and transport in three-dimensional discrete fracture matrix models using mimetic finite difference on a conforming multi-dimensional mesh. *Journal of Computational Physics*, page 111396, 2022b.
- Jeffrey D Hyman, Aric Hagberg, Dave Osthus, Shriram Srinivasan, Hari Viswanathan, and Gowri Srinivasan. Identifying backbones in three-dimensional discrete fracture networks: A bipartite graph-based approach. *Multiscale Modeling & Simulation*, 16(4):1948–1968, 2018.
- J. D. Hyman, A. Hagberg, G. Srinivasan, J. Mohd-Yusof, and H. Viswanathan. Predictions of first passage times in sparse discrete fracture networks using graph-based reductions. *Phys. Rev. E*, 96:013304, Jul 2017. doi: 10.1103/PhysRevE.96.013304.
- J. D. Hyman, M. Dentz, A. Hagberg, and P. Kang. Linking structural and transport properties in three-dimensional fracture networks. *J. Geophys. Res. Sol. Ea.*, 2019c.

- Jeffrey D Hyman. Flow channeling in fracture networks: characterizing the effect of density on preferential flow path formation. *Water Resources Research*, 56(9):e2020WR027986, 2020.
- Jeffrey D Hyman, Matthew R Sweeney, Luke P Frash, J William Carey, and Hari S Viswanathan. Scale-bridging in three-dimensional fracture networks: Characterizing the effects of variable fracture apertures on network-scale flow channelization. *Geophysical Research Letters*, 48(19): e2021GL094400, 2021.
- Aleksandra A Pachalieva, Matthew R Sweeney, Hari Viswanathan, Emily Stein, Rosie Leone, and Jeffrey D Hyman. Impact of artificial topological changes on flow and transport through fractured media due to mesh resolution. *arXiv preprint arXiv:2302.10994*, 2023.
- Gowri Srinivasan, Jeffrey D Hyman, David A Osthus, Bryan A Moore, Daniel O'Malley, Satish Karra, Esteban Rougier, Aric A Hagberg, Abigail Hunter, and Hari S Viswanathan. Quantifying topological uncertainty in fractured systems using graph theory and machine learning. *Scientific reports*, 8(1):11665, 2018.
- P.C. Lichtner, G.E. Hammond, C. Lu, S. Karra, G. Bisht, B. Andre, R.T. Mills, and J. Kumar. PFLOTRAN user manual: A massively parallel reactive flow and transport model for describing surface and subsurface processes. Technical report, (Report No.: LA-UR-15-20403) Los Alamos National Laboratory, 2015.
- David L Parkhurst, CAJ Appelo, et al. Description of input and examples for phreeqc version 3—a computer program for speciation, batch-reaction, one-dimensional transport, and inverse geochemical calculations. *US geological survey techniques and methods*, 6(A43):497, 2013.
- Diederik Jacques, Jiri Simunek, Dirk Mallants, and Martinus Th Van Genuchten. The hpx software for multicomponent reactive transport during variably-saturated flow: Recent developments and applications. *Journal of Hydrology and Hydromechanics*, pages 211–226, 2018.
- H Prommer, DA Barry, and C Zheng. Modflow/mt3dms-based reactive multicomponent transport modeling. *Groundwater*, 41(2):247–257, 2003.
- Olaf Kolditz, Sebastian Bauer, Lars Bilke, Norbert Böttcher, Jens-Olaf Delfs, Thomas Fischer, Uwe J Görke, Thomas Kalbacher, Georg Kosakowski, CI McDermott, et al. OpengEOS: an open-source initiative for numerical simulation of thermo-hydro-mechanical/chemical (thm/c) processes in porous media. *Environmental Earth Sciences*, 67:589–599, 2012.
- Jan van Der Lee, Laurent De Windt, Vincent Lagneau, and Patrick Goblet. Module-oriented modeling of reactive transport with hytec. *Computers & Geosciences*, 29(3):265–275, 2003.
- Johannes CL Meeussen. Orchestra: An object-oriented framework for implementing chemical equilibrium models. *Environmental science & technology*, 37(6):1175–1182, 2003.
- Tianfu Xu, Nicolas Spycher, Eric Sonnenthal, Guoxiang Zhang, Liange Zheng, and Karsten Pruess. Toughreact version 2.0: A simulator for subsurface reactive transport under non-isothermal multiphase flow conditions. *Computers & Geosciences*, 37(6):763–774, 2011.
- Mark D White and Mart Oostrom. Stomp subsurface transport over multiple phases version 3.0 user's guide. Technical report, Pacific Northwest National Lab., Richland, WA (US), 2003.
- GT Yeh and VS Tripathi. Hydrogeochem: A coupled model of hydrologic transport and geochemical equilibria in reactive multicomponent systems. Technical report, Oak Ridge National Lab., TN (USA), 1990.
- Carl I Steefel. Crunchflow. *Software for modeling multicomponent reactive flow and transport. User's manual*, pages 12–91, 2009.
- Danyang Su, K Ulrich Mayer, and Kerry TB MacQuarrie. Min3p-hpc: a high-performance unstructured grid code for subsurface flow and reactive transport simulation. *Mathematical Geosciences*, 53:517–550, 2021.
- Carl I Steefel, CAJ Appelo, Balveer Arora, Diederik Jacques, Thomas Kalbacher, O Kolditz, Vincent Lagneau, PC Lichtner, K Ulrich Mayer, JCL Meeussen, et al. Reactive transport codes for subsurface environmental simulation. *Computational Geosciences*, 19:445–478, 2015.
- Manuel Valera, Zhengyang Guo, Priscilla Kelly, Sean Matz, Vito Adrian Cantu, Allon G. Percus, Jeffrey D. Hyman, Gowri Srinivasan, and Hari S. Viswanathan. Machine learning for graph-based representations of three-dimensional discrete fracture networks. *Computational Geosciences*, Jan 2018b. ISSN 1573-1499. doi: 10.1007/s10596-018-9720-1. URL <https://doi.org/10.1007/s10596-018-9720-1>.
- Shriram Srinivasan, Eric Cawi, Jeffrey Hyman, Dave Osthus, Aric Hagberg, Hari Viswanathan, and Gowri Srinivasan. Physics-informed machine learning for backbone identification in discrete fracture networks. *Computational Geosciences*, 24:1429–1444, 2020.
- Matthew R. Sweeney, Carl W. Gable, Satish Karra, Philip H. Stauffer, Rajesh J. Pawar, and Jeffrey D. Hyman. Upscaled discrete fracture matrix model (UDFM): an octree-refined continuum representation of fractured porous media. *Computational Geosciences*, 24(1):293–310, 2020. ISSN 15731499. doi: 10.1007/s10596-019-09921-9.
- H. S. Viswanathan, J. Ajo-Franklin, J. T. Birkholzer, J. W. Carey, Y. Guglielmi, J. D. Hyman, S. Karra, L. J. Pyrak-Nolte, H. Rajaram, G. Srinivasan, and D. M. Tartakovsky. From fluid flow to coupled processes in fractured rock: Recent advances and new frontiers. *Reviews of Geophysics*, 60(1):e2021RG000744, 2022. e2021RG000744 2021RG000744.
- Johannes Krotz, Matthew R. Sweeney, Carl W. Gable, Jeffrey D. Hyman, and Juan M. Restrepo. Variable resolution poisson-disk sampling for meshing discrete fracture networks. *Journal of Computational and Applied Mathematics*, 407:114094, 2022.
- LaGrIT. Los Alamos Grid Toolbox, (LaGrIT) Los Alamos National Laboratory. <http://lagrit.lanl.gov>, 2013.
- Svensk Kärnbränslehantering AB. Data report for the safety assessment SR-site (TR-10-52). Technical report, Svensk Kärnbränslehantering AB, 2010.
- S Karra, N Makedonska, HS Viswanathan, SL Painter, and JD Hyman. Effect of advective flow in fractures and matrix diffusion on natural gas production. *Water Resour. Res.*, 51(10):8646–8657, 2015.
- A. Frampton, J. D. Hyman, and Liangchao Zou. Advective transport in discrete fracture networks with connected and disconnected textures representing internal aperture variability. *Water Resour. Res.*, 55(7):5487–5501, 2019.
- N. Makedonska, J. D. D Hyman, S. Karra, S. L Painter, C. W. W Gable, and H. S Viswanathan. Evaluating the effect of internal aperture variability on transport in kilometer scale discrete fracture networks. *Adv. Water Resour.*, 94:486–497, 2016.
- SY Greer, JD Hyman, and Daniel O'Malley. A comparison of linear solvers for resolving flow in three-dimensional discrete fracture networks. *Water Resources Research*, 58(4):e2021WR031188, 2022.
- Donald M Fisher and Susan L Brantley. Models of quartz overgrowth and vein formation: deformation and episodic fluid flow in an ancient subduction zone. *Journal of Geophysical Research: Solid Earth*, 97(B13):20043–20061, 1992.

- Alexis Navarre-Sitchler, Susan L Brantley, and Gernot Rother. How porosity increases during incipient weathering of crystalline silicate rocks. *Reviews in Mineralogy and Geochemistry*, 80(1):331–354, 2015.
- Roland Wollast and Lei Chou. *Rate Control of Weathering of Silicate Minerals at Room Temperature and Pressure*, pages 11–32. Springer Netherlands, Dordrecht, 1988. ISBN 978-94-009-3071-1.
- Jeremy Watt, Reza Borhani, and Aggelos K Katsaggelos. *Machine learning refined: Foundations, algorithms, and applications*. Cambridge University Press, 2020.
- Tin Kam Ho. Random decision forests. In *Proceedings of 3rd international conference on document analysis and recognition*, volume 1, pages 278–282. IEEE, 1995.
- Scikit learn random forest regression model documentation. <https://scikit-learn.org/>, Accessed: 2023-09-19.
- Sigmund Mongstad Hope, Philippe Davy, Julien Maillot, Romain Le Goc, and Alex Hansen. Topological impact of constrained fracture growth. *Frontiers in Physics*, 3:75, 2015.
- Christian André Andresen, Alex Hansen, Romain Le Goc, Philippe Davy, and Sigmund Mongstad Hope. Topology of fracture networks. *Frontiers in Physics*, 1:Art–7, 2013.
- Aric A Hagberg, Daniel A Schult, and P Swart. Exploring network structure, dynamics, and function using networkx. In *Proceedings of the 7th Python in Science Conferences (SciPy 2008)*, volume 2008, pages 11–16, 2008.
- Harald Abelin, Lars Birgersson, Luis Moreno, Hans Widén, Thomas Ågren, and Ivars Neretnieks. A large-scale flow and tracer experiment in granite: 2. results and interpretation. *Water Resour. Res.*, 27(12):3119–3135, 1991.
- H Abelin, I Neretnieks, S Tunbrant, and L Moreno. *Final report of the migration in a single fracture: experimental results and evaluation*. Nat. Genossenschaft fd Lagerung Radioaktiver Abfälle, 1985.
- Andrew Frampton and Vladimir Cvetkovic. Numerical and analytical modeling of advective travel times in realistic three-dimensional fracture networks. *Water Resour. Res.*, 47(2), 2011.
- Anders Rasmuson and Ivars Neretnieks. Radionuclide transport in fast channels in crystalline rock. *Water Resources Research*, 22(8):1247–1256, 1986.
- Diane Doolaege, Philippe Davy, Jeffrey D Hyman, and Caroline Darcel. Graph-based flow modeling approach adapted to multiscale discrete-fracture-network models. *Physical Review E*, 102(5):053312, 2020.
- Jac M Anthonisse. The rush in a directed graph. *Stichting Mathematisch Centrum. Mathematische Besliskunde*, 1971.
- Linton C Freeman. A set of measures of centrality based on betweenness. *Sociometry*, pages 35–41, 1977.
- Ulrik Brandes and Daniel Fleischer. Centrality measures based on current flow. In *Annual symposium on theoretical aspects of computer science*, pages 533–544. Springer, 2005.
- Mark EJ Newman. A measure of betweenness centrality based on random walks. *Social networks*, 27(1):39–54, 2005.
- S Karra, D O'Malley, JD Hyman, HS Viswanathan, and G Srinivasan. Modeling flow and transport in fracture networks using graphs. *Physical Review E*, 97(3):033304, 2018.